The Planetary Science Journal, 6:241 (24pp), 2025 October https://doi.org/10.3847/PSJ/ae0296

Modeling Low-temperature Plasmas Simulating Titan's Atmosphere

David Dubois[1,2,4], Alexander W. Raymond[3], Ella Sciamma-O'Brien[1], and Farid Salama[1]
[1] NASA Ames Research Center, Space Science & Astrobiology Division, Astrophysics Branch, Moffett Field, CA, USA; david.f.dubois@nasa.gov
[2] Bay Area Environmental Research Institute, Moffett Field, CA, USA
[3] Jet Propulsion Laboratory, California Institute of Technology, Pasadena, CA, USA
Received 2025 June 16; revised 2025 August 13; accepted 2025 August 27; published 2025 October 24

Abstract

In the study presented here, we model the gas phase chemistry induced by plasma discharge at low temperatures (150 K) in the NASA Ames COSmIC Simulation Chamber (COSmIC) using a 1D multifluid plasma model named COSmIC Plasma Reactivity and Ionization Simulation Model. Our model incorporates an extensive chemical reaction network to simulate the neutral–neutral and ion–neutral reactions occurring in the COSmIC experiments when using N_2–CH_4-based gas mixtures relevant to Titan's atmosphere. Our reaction network now includes crucial reactions involving the first electronically excited state of atomic nitrogen, recent electron collision cross sections, and radical chemistry. In particular, we have investigated the influence of C_2H_2 on the gas phase polymeric growth and the elemental composition of the chemical products, and we have compared our findings to recently published solid phase analyses. The modeling results are consistent with experimental measurements of N_2–CH_4–C_2H_2 plasmas on COSmIC, showing the production of C_6Hx intermediates and precursors of larger organics, as well as methanimine in small concentration. Our numerical results point to cationic pathways enabling efficient intermediate-sized and nitrogen-rich C_2H_2-driven chemistry driving tholin production. Comparison of the modeled gas phase elemental composition with the elemental composition of the solid phase samples produced in COSmIC reveals similar trends, with C/N increasing when C_2H_2 is present in the gas mixture. Finally, our results demonstrate the importance of such synergistic studies using low-temperature plasma chemistry experiments combined with modeling efforts to improve our understanding of cold planetary environments.

Unified Astronomy Thesaurus concepts: Titan (2186); Laboratory astrophysics (2004); Astronomical models (86); Reaction models (2231)

Materials only available in the online version of record: machine-readable table

1. Introduction

Ion–neutral molecular reactions play an important role in shaping the chemistry in solar system and planetary ionospheres (e.g., W. T. Huntress 1977; R. G. Harrison & H. Tammet 2008; M. Larsson et al. 2012; V. Vuitton et al. 2019; M. L. Wong et al. 2023). These reactions involve the interaction between ions and neutral molecules, which can result in the formation of various chemical species. For example, in the atmosphere of Mars, ion–neutral reactions are important for the production of nitrogen oxides where charge transfer processes from N_2^+, Ar^+, and CO^+ represent key ionization pathways of CO_2 (M. Larsson et al. 2012). In the outer solar system, where nitrogen- and hydrocarbon-based chemistry dominates, cation-neutral reactivity has long been thought to play a role in the transition from the gas phase to the solid phase. Characterizing these reactions has been crucial for understanding the thermal, chemical, and physical processes that occur in the solar system and developing accurate models of these environments (M. Larsson et al. 2012 and references therein).

Titan, Saturn's largest moon, is the only known moon to have its own dense atmosphere, mostly composed of molecular nitrogen, N_2 (∼95%), and methane, CH_4 (∼2%–5%). This reducing atmosphere consists of five main atmospheric layers (troposphere, stratosphere, mesosphere, thermosphere, and exosphere) hosting planetary-like dynamical, thermal, chemical, and seasonal variations on a global scale. The formation of the haze surrounding Titan is ultimately controlled by the gas phase molecular precursors produced in the upper atmosphere resulting from high-altitude N_2 and CH_4 photolysis and radiolysis. These precursors consist of hydrocarbon radicals (e.g., CH_2, CH_3) and more complex hydrocarbons, nitriles, and polycyclic aromatic hydrocarbons (PAHs; J. H. Waite et al. 2007). Energetic sources triggering high-altitude chemistry include solar UV photons, solar X-rays, and Saturn's magnetospheric energetic electrons (V. A. Krasnopolsky 2014). The Cassini spacecraft studied Titan for 13 yr and directly measured the molecular mass of ions for the first time in Titan's upper atmosphere (J. H. Waite et al. 2007; F. J. Crary et al. 2009). These observations uncovered the complexity of Titan's upper atmospheric chemistry, consisting of radicals, neutrals, positive and negative ions, and the preliminary stages of solid haze particle formation. In some cases, the measured abundances of certain short-lived ions such as CH_4^+, $HCNH^+$, and $C_2H_5^+$ exceeded the predicted abundances determined by previous models (e.g., J. Cui et al. 2009a). On the other hand, the abundance of some heavy hydrocarbons and N-bearing neutral molecules measured by the Cassini Ion Neutral Mass Spectrometer (INMS) were found to be lower than what ion–neutral models had estimated (J. Cui et al. 2009b and references therein). These observations

[4] Corresponding author.

highlighted the role of magnetospheric electron precipitation on Titan's nightside and diurnal variations that directly impact the molecular distribution in the upper atmosphere.

Simulating Titan's ionospheric chemistry in the laboratory constrains the chemical precursors of haze particles formed at high altitude. These particles descend to lower altitudes where they can act as condensation nuclei in the lower stratosphere and where they may settle to the surface. Simulating upper atmospheric chemistry can thus provide insight into the chemical composition in the lower atmosphere.

Chemical models have helped explain the gas phase chemistry that produces the neutral and ion precursors of aerosols found in Titan's atmosphere (e.g., V. Vuitton et al. 2019). Alongside those models, laboratory experiments have helped in vetting the reaction networks through the study of specific channels involving neutral and charged molecular species. Furthermore, photochemical and microphysical models have investigated the dusty nature of Titan's ionosphere (>900 km in the atmosphere) and characterized the interaction between the aerosols and charged particles (P. Lavvas et al. 2013). More specifically, by using a wide array of energy sources and coupling extensive lists of ion–neutral reactions, models have given insights into the first steps linking small hydrocarbons with larger molecules (M. Dobrijevic et al. 2016; J. C. Loison et al. 2017; V. Mukundan & A. Bhardwaj 2018; V. Vuitton et al. 2019). Ion–molecule reactions are thought to be directly relevant to aerosol growth and are controlled by the relative abundances of the two initial neutral main constituents, N_2 and CH_4 (P. Lavvas et al. 2013). The dissociative ionization of CH_4 results in the formation of CH_3^+, an ion predicted (V. G. Anicich 2003) to participate in the production of the first light hydrocarbons, such as $C_2H_5^+$, occurring on both the nightside and dayside of Titan:

$$CH_3^+ + CH_4 \longrightarrow C_2H_5^+ + H_2. \quad (1)$$

Following Reaction (1), a long suite of dissociative recombination reactions have been predicted to occur, forming acetylene (C_2H_2; Reaction (2)), ethylene (C_2H_4; Reaction (3)), and, eventually, benzene (C_6H_6; Reaction (4)), the first and only six-membered ring that has been discovered in Titan's lower atmosphere clouds to date (A. Coustenis et al. 1999; V. Vuitton et al. 2008; S. Vinatier et al. 2018). Other unidentified emission features were identified as potential carriers of PAHs (B. M. Dinelli et al. 2013; M. López-Puertas et al. 2013). Benzene is expected to serve as a potential seed for larger macromolecules and aromatics, for example, by radical-phenyl pathways (V. Vuitton et al. 2008). Larger molecular structures (>C9 hydrocarbons) formed through dissociative recombinations at lower altitudes (<1200 km) have also been proposed (e.g., F. J. Crary et al. 2009) to be possible precursors to PAHs. Both cation and anion pathways have then been studied to explain the presence of these large precursors observed by Cassini (J. Žabka et al. 2009, 2012):

$$C_2H_5^+ + e^- \longrightarrow C_2H_2 + H_2 + H, \quad (2)$$

$$C_2H_5^+ + e^- \longrightarrow C_2H_4 + H, \quad (3)$$

$$C_6H_7^+ + e^- \longrightarrow C_6H_6 + H. \quad (4)$$

While dissociative recombination constitutes a mechanism for the loss of certain ions, ion–neutral reactions play a major role in the formation of ions. For instance, both ion–neutral and dissociative recombination are proposed to explain the production and loss of cyclic $C_3H_3^+$, respectively, which itself depends on the presence of CH_4 and C_2H_2 (V. Vuitton et al. 2019). Reactions involving $C_3H_3^+$ can produce benzene. Note that lower in Titan's atmosphere, C_3H_3 dimerization can also produce benzene (V. Vuitton et al. 2008; M. Larsson et al. 2012).

Along with hydrocarbons and PAHs, nitriles are among the most abundant compounds in Titan's atmosphere. INMS measurements coupled with photochemical models yielded peak mole fractions of 2×10^{-4} for HCN, the most abundant photochemically produced nitrile, and $\sim 10^{-6}$ for $HCNH^+$ at 1100 km (M. Dobrijevic et al. 2016; V. Vuitton et al. 2019). The nitriles produced in the upper atmosphere have relatively larger proton affinities, thus leading to their more stable closed shell cation counterparts. HCN, for example, is formed through neutral–neutral reactions in the upper atmosphere, while $HCNH^+$ forms through direct proton transfer to HCN or $N^+ + CH_4$. Other N-bearing molecules, such as acetonitrile (CH_3CN) and cyanoacetylene (HC_3N), are highly reactive and play a significant role in the nitrogen-based ion–neutral chemistry of Titan's atmosphere (V. Vuitton et al. 2007). In the ionosphere, these neutral and cation nitriles can undergo various reactions with other ions, electrons, and free radicals, leading to the formation of more complex organic molecules in the ionosphere (J. L. Berry et al. 2019; V. Vuitton et al. 2019; D. Dubois et al. 2020; N. Carrasco et al. 2022; C. A. Nixon 2024).

Some of these compounds are also of astrobiological interest, such as methylamine $CH_3NH_2^+$, a precursor to amino acids in the long chain of HCN hydrogenation reactions (X. Gu et al. 2009; P. C. Singh et al. 2010; P. Theule et al. 2011). HCN itself is the smallest neutral containing a CN moiety, which is key in the amino acid formation process (P. Theule et al. 2011; J. A. Noble et al. 2013). Ion–neutral reactivity therefore plays a key role at every stage of Titan's chemical reactivity: (i) the degradation and recombination of small neutrals and free radicals; (ii) the formation of larger molecules, PAHs, and haze particles; and (iii) the formation of putative molecules of astrobiological interest. However, the processes involved in coupling ion and neutral chemistry and aerosol production are complicated and an area of ongoing study.

Laboratory experiments have been conducted to simulate Titan's atmospheric chemistry using plasmas created by different energy sources (e.g., UV-induced photochemistry, plasma discharges) to induce chemistry in various precursor gas mixtures representative of Titan's atmospheric composition (e.g., T. W. Scattergood et al. 1989; C. Sagan et al. 1992; H. Imanaka et al. 2004; C. Szopa et al. 2006; S. Pilling et al. 2009; M. L. Cable et al. 2012; N. Carrasco et al. 2012; F. Raulin et al. 2012; J. Žabka et al. 2012; I. Couturier-Tamburelli et al. 2014; E. Sciamma-O'Brien et al. 2014; S. M. Hörst et al. 2018; J. Bourgalais et al. 2019, 2020, 2021; D. Dubois et al. 2019a, 2019b). These experiments along with the development of photochemical and microphysical models have helped better constrain the chemical pathways leading to the formation of larger molecules and solid particles in Titan's atmosphere and have substantially advanced our understanding of the chemistry occurring in Titan's ionosphere (D. Dubois 2025). However, these numerical simulations by models have faced some obstacles due to a limited number of reactions with known reaction rates at Titan-relevant temperatures.

To further advance our understanding of Titan's ionospheric chemistry, experiments were conducted with the COSmIC Simulation Chamber at NASA Ames Research Center to investigate low-temperature (150 K) gas phase chemistry in ionized conditions using a plasma discharge in the stream of jet-cooled expansions of N_2–CH_4-based gas mixtures. The COSmIC experiment is designed to simulate low-temperature chemistry in conditions relevant to Titan and planetary atmospheres (F. Salama et al. 2017). The general goal of our study (i.e., combining chemistry modeling with experimental measurements) is to determine specific relevant pathways to understand the chemistry occurring in the COSmIC experimental setup when simulating Titan's atmospheric chemistry and is therefore of interest for the Titan/planetary community.

By comparing the COSmIC experimental data to synthetic mass spectra generated by the COSmIC Plasma Reactivity and Ionization Simulation Model (CO-PRISM), we can (1) validate the chemical network considered in CO-PRISM, (2) identify specific pathways or molecules that are missing to fit the experimental data and accordingly implement changes to the model, (3) quantify and identify the species produced in the plasma, (4) assess the impact of specific chemical pathways on the resulting chemical products, and finally, (5) guide and optimize future COSmIC experiments relevant to Titan's atmosphere (e.g., what chemical pathways produce specific molecules). The need for new COSmIC experiments focusing on specific chemical pathways to help in the interpretation of Cassini observations was demonstrated in E. Sciamma-O'Brien et al. (2014).

In these experiments, the gas phase was characterized by mass spectrometry to monitor the formation of larger molecular products in the plasma discharge (E. Sciamma-O'Brien et al. 2014, 2017). In parallel, a 1D multifluid chemical network model was developed to simulate the chemical reactivity occurring in the plasma discharge (A. W. Raymond et al. 2018). This model enables generating simulated mass spectra that can then be compared to experimental mass spectra. In this study, we incorporate updated reaction rates and a total of 45 newly updated reaction pathways into this model, now called CO-PRISM. We study the impact of changing plasma parameters on the ion chemistry, expanding on the investigation of the plasma parameter space impact on the chemistry from previous studies. A total of 11 N_2–CH_4-based initial gas mixture conditions are explored. Furthermore, the updated model is used to calculate the C/N elemental composition of the gas phase products, which we present below with a comparison to recently published solid phase C/N ratios of Titan aerosol analogs produced in COSmIC. We also discuss the result of a sensitivity analysis conducted with our model considering various energy levels (voltage on the plasma source) and show how the chemistry in COSmIC is affected by electrode potential. In addition, the mole fractions of six major ions (CH^+, CH^{3+}, $C_2H_3^+$, $C_2H_5^+$, $C_4H_3^+$, and $C_5H_5^+$) produced in the plasma discharge are computed, and we show their evolution in time in the plasma channel and their sensitivity to the initial composition of the gas mixture. Finally, extracted mass spectra are compared to previous laboratory and numerical simulations to demonstrate the importance of combining experiments and modeling to improve our understanding of planetary environments.

2. Simulation of Titan's Atmospheric Chemistry

2.1. COSmIC

The COSmIC facility was developed at NASA Ames Research Center to simulate astrophysical and planetary environments at low temperature (F. Salama et al. 2017). Among these environments, Titan's low-temperature (150 K) gas phase chemistry in plasma conditions was of particular interest and led to the development of targeted experiments on COSmIC (e.g., E. Sciamma-O'Brien et al. 2014). In the COSmIC setup, a pulsed discharge nozzle (PDN) is used to (1) cool down a gas mixture by expanding it through a thin 127 μm $\times$ 10 cm slit and (2) generate a plasma discharge in the stream of the jet-cooled gas expansion by applying a high voltage onto cathodes placed in the stream of the expansion (see Figures 1(a) and (b); J. R. M. Remy et al. 2003; B. H. Broks et al. 2005a; B. H. P. Broks et al. 2005b).

The COSmIC PDN source has been effectively used to simulate analogous conditions to astrophysical and planetary environments and study both the gas and solid phase. Molecular species present in the plasma expansion have been monitored by reflectron time-of-flight (TOF) mass spectrometry (C. L. Ricketts et al. 2011; C. S. Contreras & F. Salama 2013; E. Sciamma-O'Brien et al. 2014) and cavity ring-down spectroscopy (X. Tan & F. Salama 2005; L. Biennier et al. 2006b; S. Bejaoui & F. Salama 2019; S. Bejaoui et al. 2023). Solid particles, analogs of planetary aerosols (E. Sciamma-O'Brien et al. 2017, 2023; E. S. O'Brien et al. 2019; M. Nuevo et al. 2022) and cosmic grains (F. Salama et al. 2017; L. G. Marin et al. 2020; E. Sciamma-O'Brien et al. 2020), have been produced in the plasma expansion and analyzed ex situ with various techniques ranging from scanning electron microscopy and infrared spectroscopy to X-ray absorption near edge structure spectroscopy (XANES).

In COSmIC, nitrogen-methane-based gas mixtures are used to simulate Titan's atmospheric chemistry. The expansion of the pulsed gas in the cavity between the anode and the cathode results in the cooling of the gas mixture down to low Titan-like temperatures relevant to the upper atmosphere ($\sim$150 K) before inducing the chemical breakdown within the plasma discharge (L. Biennier et al. 2006b). The short residence time of the gas in the plasma discharge (less than 4 μs) results in a truncated chemistry that enables simulating and studying the first steps in the chemical reaction pathways of Titan's atmosphere.

In the study presented here, we focus on first updating the numerical model that simulates the chemistry in the COSmIC/Titan Haze Simulation (THS) experiments and assess the impact of changing some of the modeling parameters on the numerical results. We then compare our new simulated mass spectra to those obtained experimentally and using the first version of CO-PRISM (E. Sciamma-O'Brien et al. 2014; A. W. Raymond et al. 2018). Table 1 provides a summary of the parameters used for the experimental and numerical results discussed in this paper.

2.2. CO-PRISM

CO-PRISM is the 1D numerical model first developed by A. W. Raymond et al. (2018) to simulate the chemical network in a plasma discharge (Figure 1(b)) generated with the COSmIC PDN in N_2–CH_4-based initial gas mixtures. It is a modular model that can be applicable to a wide range of

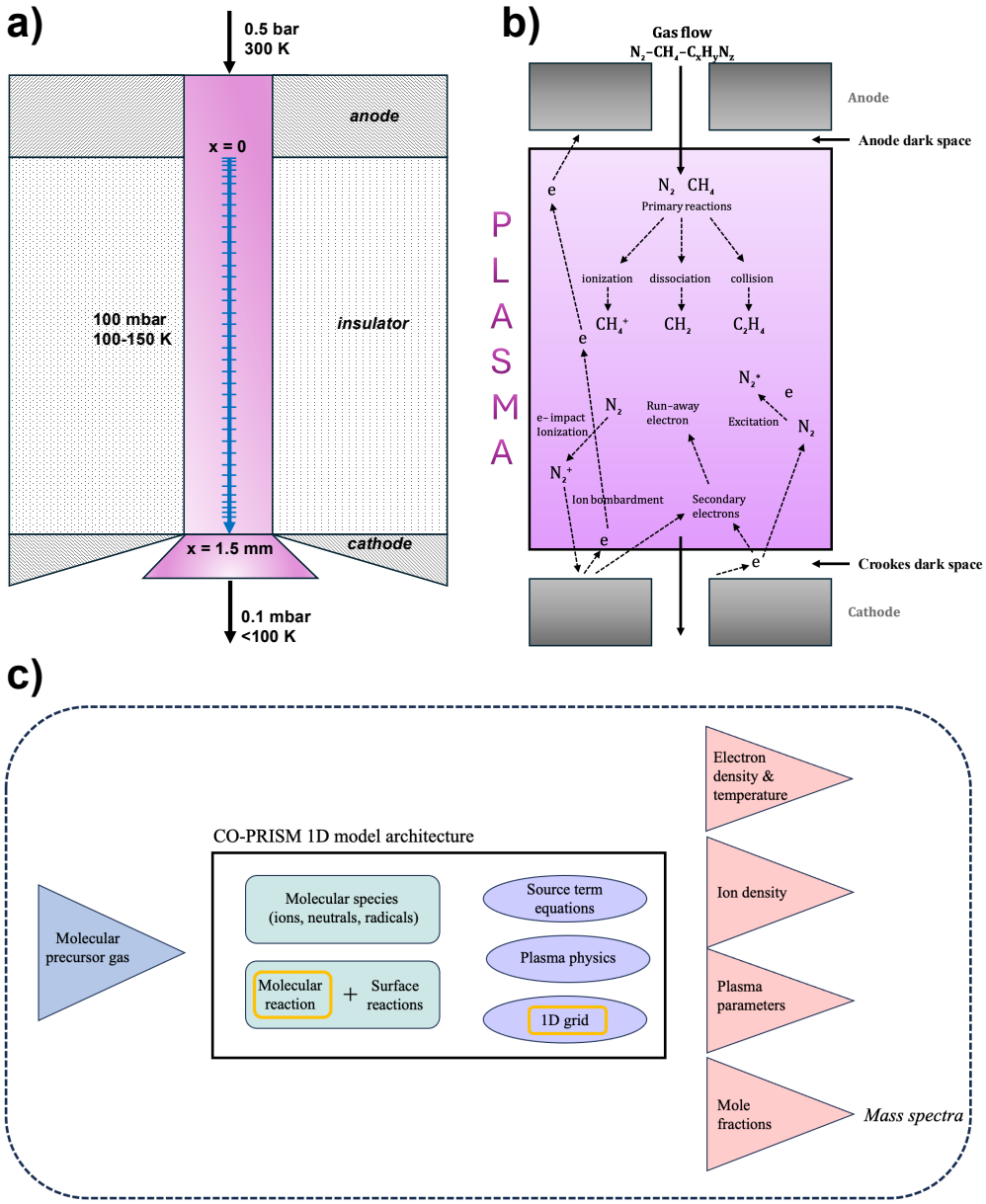

Figure 1. (a) Cross-section schematic view of the THS plasma channel (not to scale). The pathway along which reactions are calculated by the model in the plasma channel is indicated in blue. The temperature inside the plasma cavity is on the order of $T = 150$ K (L. Biennier et al. 2006a; E. Sciamma-O'Brien et al. 2014). (b) Top-view cross-section schematic view of the plasma cavity (not to scale) indicating the dominant collisional processes occurring in the plasma and controlling the formation of the first building blocks leading to larger products, illustrated in the case of a N_2–CH_4-based atmosphere relevant to Titan. (c) Simplified schematic representation of CO-PRISM. Each simulation is controlled by the initial precursor gas composition (blue triangle). Green boxes correspond to the chemical input parameters (list of species, molecular reactions, and surface reactions), purple ellipses correspond to plasma physics and grid geometry parameters, and outputs are represented with red triangles. The model parameters that were updated and modified in the study presented here are circled in orange. Synthetic mass spectra can then be retrieved from the computed mole fractions.

planetary and astrophysical environments simply by adding the relevant reactions for the gas mixture used in the COSmIC experiments. The goal of the Titan CO-PRISM in its present form is to quantify the molecular species (neutrals and positive ions) produced in the COSmIC experiments and generate synthetic mass spectra comparable to experimentally measured mass spectra acquired with COSmIC's TOF mass spectrometer (C. L. Ricketts et al. 2011; E. Sciamma-O'Brien et al. 2014) but also to mass spectra generated by photochemical models (e.g., V. Vuitton et al. 2019) and in situ Cassini mass spectra (e.g., J. H. Waite et al. 2007). The TOF is equipped with a polarized skimmer that attracts ions into the instrument and detects them directly without fragmentation. As stated above, the gas phase products measured by the TOF can help us better characterize the mixture-dependent composition, thus guiding future experiments needed to help the interpretation of Cassini observations.

In CO-PRISM, plasma physics parameters such as the ionization fractions and the electron temperature are calculated using a fluid mechanical approach (A. W. Raymond et al. 2018) following previous numerical investigations and characterization of the plasma discharge produced in the COSmIC PDN (J. R. M. Remy et al. 2003; B. H. Broks et al. 2005a; B. H. P. Broks et al. 2005b) and detailed hereafter. CO-PRISM

Table 1
List of the Parameters Used in the Experimental and Modeling Gas Phase Studies for Various N_2–CH_4-based Simulated Atmospheres

Gas Mixture	Ratio	Gas Flow (sccm)	Voltage (V)	Experiment[a]	CO-PRISM (2018)[b]	CO-PRISM (2025)
N_2–CH_4	99:1	2000	1000	⋯	⋯	x
N_2–CH_4	95:5	2000	700	⋯	x	x
N_2–CH_4	95:5	2000	800	⋯	x	x
N_2–CH_4	95:5	2000	1000	x	x	x
N_2–CH_4	90:10	2000	800/1000	x	x	x
N_2–CH_4–C_2H_2	85:10:5	2000	800/1000	x	x	x
N_2–CH_4–$_2H_4$	85:10:5	2000	800/1000	x	x	x
N_2–CH_4–C_2H_6	85:10:5	2000	1000	⋯	⋯	x
N_2 − CH_4 − HCN	85:10:5	2000	1000	⋯	⋯	x
N_2–CH_4–CH_2NH	85:10:5	2000	1000	⋯	⋯	x
N_2–CH_4–NH_3	85:10:5	2000	1000	⋯	⋯	x

Note. Gas flows are provided in standard cubic centimeters. The voltage applied to the cathode to generate the plasma is provided in volts. Only ultra-high-purity gases were used for the experimental study, and mixing ratios and flows were controlled by MKS 1479 mass flow controllers.
[a] E. Sciamma-O'Brien et al. (2014).
[b] A. W. Raymond et al. (2018).

also takes into account the abnormal glow nature of the COSmIC plasma discharge (e.g., J. R. M. Remy et al. 2003), i.e., an electron density at the higher end of the range typically deemed normal for glow discharges.

2.2.1. CO-PRISM

Figure 1(c) shows a simplified flowchart representation of the CO-PRISM 1D model. The main inputs consist of a list of molecular species, the molecular reactions that contribute to their formation or destruction in the plasma (neutral–neutral and neutral–ion with associated reaction coefficients), and a suite of surface reactions (neutralization reactions and secondary electrons formed near the cathode).

The CO-PRISM architecture uses a 1D grid with a user-defined grid size. In this study, the grid size was increased to 100 nodes distributed along an arithmetic sequence to help improve the sensitivity of our calculations (see the blue grid in Figure 1(a)).

The model outputs include the molar fractions of all the species (cations, neutrals, radicals) formed in the simulated plasma discharge along the plasma channel. Mass spectra can subsequently be computed from the molar fraction obtained at a given position in the plasma channel and compared against the measured spectra taken by mass spectrometry. Isotopes are not presently included in CO-PRISM. This is an element that we are considering for future development.

In CO-PRISM, the electron density and electron energy density outputs are derived following B. H. Broks et al. (2005a) and B. H. P. Broks et al. (2005b) from the following equations, respectively:

$$R_e = \frac{\partial n_e}{\partial t} - \nabla \cdot [(\mu_e \cdot E) n_e + \nabla (D_e n_e)] \tag{5}$$

and

$$S_\varepsilon = \frac{\partial n_\varepsilon}{\partial t} - \nabla \cdot [(\mu_\varepsilon \cdot E) n_\varepsilon + \nabla (D_\varepsilon n_\varepsilon)] + E \cdot [(\mu_e \cdot E) n_e + \nabla (D_e n_e)], \tag{6}$$

where the subscripts e and ε correspond to the electrons and the electron energy density (thermionic energy) in the discharge, respectively. R_e is the source term for electrons, S_ε is the energy source term accounting for inelastic collisions, E is the electric field, D is the diffusivity, and μ is the mobility (G. J. Hagelaar & L. C. Pitchford 2005). The concentrations of heavy species (i.e., neutrals, ions, and radicals) are calculated using the following formalism:

$$\rho \frac{\partial \omega_k}{\partial t} + \rho (u \cdot \nabla) \omega_k = \nabla \cdot \left[\rho \omega_k D_k \frac{\nabla \omega_k}{\omega_k} - z_k \mu_k E \right] + R_k, \tag{7}$$

where ω_k represents the mass fraction of the k_{th} molecular species and R_k corresponds to the source term for heavy species. The mixture-average diffusion coefficient D_k is considered negligible ($D_k = 0$) since the supersonic expansion dominates the continuous flow within a plasma pulse (A. W. Raymond et al. 2018). For each species, the source term R_k is obtained by computing a network of chemical rate equations. A. W. Raymond et al. (2018) simplified the B. H. Broks et al. (2005a) and B. H. P. Broks et al. (2005b) 2D model into the 1D CO-PRISM in order to allow for a larger chemical network to be simulated. Calculations are conducted along the x-axis (A. W. Raymond et al. 2018), with the anode occupying the assigned inlet position and the cathode the

outlet position (see Figure 1(a)). For each simulation, the initial gas composition mixing ratio (N_2, CH_4, with or without the addition of other trace hydrocarbons used as precursors) is defined in the model to be representative of the Titan COSmIC experiments we want to compare the numerical outputs to. In addition, following A. W. Raymond et al. (2018), a small number of $N_2(X, \nu = 0)^+$ ions are added to the initial gas mixture in the model to insure quasi-neutrality with the seed electrons (Equation (5)). All other species except the initial N_2–CH_4-based carrier gas are initialized with a null abundance.

The model also includes surface reactions to account for ions near the inlet diffusing into the anode as well as heavy species loss, neutralization of ions, and the generation of secondary electrons at the cathode. The rate constants of the surface reactions are calculated following (H. Motz & H. Wise 1960)

$$r = k_s^f \prod_{k=1}^{Q} c_k^{\nu}, \tag{8}$$

where the forward rate constant k_s^f is calculated with

$$k_s^f = \left(\frac{\gamma_f}{1 - \gamma_f/2}\right) \frac{\prod \sigma_j^{\nu} j1}{(\Gamma_{\rm tot})^m 4} \sqrt{\frac{8RT}{\pi M_k}}, \tag{9}$$

where T is the local temperature, M_k is the molar mass of the $k_{\rm th}$ ionic species, R is the ideal gas constant, and Γ is the surface site concentration. γ_f is the sticking coefficient and, as explained in A. W. Raymond et al. (2018), is maintained constant at a value of 1 across the plasma channel in the model to focus on the chemistry occurring in the plasma more than on wall effects. A total of 151 surface reactions are currently present in the model, compared to 64 in A. W. Raymond et al. (2018). The model also parameterizes a secondary emission effect (i.e., a secondary emission coefficient and mean energy of secondary electrons). Electron impact reactions follow electron collision cross sections and include excitation, attachment, ionization, and elastic reactions.

Every reaction considered here is irreversible according to the following time-dependent rate parameterization based on Equation (8),

$$r = k^f \prod_{k=1}^{Q} c_k^{\nu}, \tag{10}$$

where the rate constants k^f ($m^3/(s \cdot mol)$) determined for each reaction are taken into account:

$$k^f = \gamma \int_0^{\infty} \epsilon \sigma_k(\epsilon) f(\epsilon) d\epsilon. \tag{11}$$

As described in A. W. Raymond et al. (2018), to accommodate positive ions present near the inlet diffusing into the anode, we use a surface reaction at the inlet boundary that acts both as sink and source term. To account for heavy species loss, ion neutralization (e.g., $CH_4^+ \longrightarrow CH_4$), and the generation of secondary electrons at the cathode, we use an open boundary condition and a point surface reaction at the outlet/cathode. Secondary electrons are generated according to a secondary emission coefficient determined to be 0.025 (A. V. Phelps & Z. L. Petrovic 1999). An illustrative view of the dominant chemical processes that occur in the plasma channel is shown in Figure 1. The dark spaces near the anode and cathode help maintain the quasi-neutrality of the plasma, while rapid free electrons are accelerated in the plasma channel inducing electron impact ionization and dissociative reactions. Secondary electrons are produced at the cathode with a rate fixed by the secondary emission coefficient (J. R. M. Remy et al. 2003; B. H. P. Broks et al. 2005b; A. W. Raymond et al. 2018).

In this study, calculations were conducted along a 1D grid with 100 node points (increased from 40 in A. W. Raymond et al. 2018). Node distribution is user-defined, and its sequence follows a symmetric and arithmetic distribution between the anode and cathode (Figure 1(a)). Our grid contains a maximum element growth rate of 1.3 and a maximum element size of 1.01×10^{-4} m. The 1D space chosen by A. W. Raymond et al. (2018) accommodates the larger number of reactions compared to the 2D model used by B. H. P. Broks et al. (2005b) while keeping the computation tractable. The computational grid is based on the COSmIC/THS PDN geometry (Figure 1(a)), where the gas mixture flows through a 100 mm long and 127 μm tall inlet at the anode. At the outlet, the cathode is represented by two elkonite conductors. The inner region (i.e., plasma channel or cavity) is confined by two alumina plates (acting as an insulator) and is 1.5 mm wide. The analysis of plasma properties and molecular composition was performed along the width of this plasma channel.

2.2.2. Reaction Network Refinements

The reaction network in A. W. Raymond et al. (2018) tracked 155 molecular species and contained 249 reactions including electron impact, ion–neutral, and neutral–neutral reactions. It also contained 64 surface reactions, neutralizing ions and producing secondary electrons. CO-PRISM now contains 294 electron impact and bimolecular reactions and 67 surface reactions for a total of 168 species. As described below, the previous CO-PRISM reaction network did not include key electron impact reactions relevant to cold plasma discharges involving C_2H_2, C_2H_4, and C_2H_6.

In the present study, we have updated the reaction rates to refine CO-PRISM and addressed gaps by

1. updating the reaction rates of 77 reactions in accordance with new values from V. Vuitton et al. (2019),
2. including key electron impact reactions relevant to hydrocarbon-based (C_2H_2, C_4H_2, and C_6H_2) plasma discharges,
3. including key reactions forming NH_3 and its derivatives relevant to Titan's upper atmosphere, and
4. including key reactions involving the first electronically excited state of atomic nitrogen and methanimine (CH_2NH) and the very important NH intermediate radical.

In order to expand on the scope of the plasma conditions, we updated the model with a set of three electron impact dissociative ionization reactions for C_2H_2, C_4H_2, and C_6H_2 (see R1, R2, and R3 of Table 2) and a total of 45 new reactions. These, including electron impact excitation reactions in particular, are key for characterizing nonequilibrium gases (W. M. Huo et al. 2015). Electron collision cross-section data for R1, R2, and R3 are obtained from C. Tian & C. R. Vidal (1998) and K. De Bleecker et al. (2006b). The global networks including all neutral–ion pathways and all neutral-only

Table 2
List of 45 New Reactions Added to the New Version of the CO-PRISM Scheme Along with Their Associated Reactions Rates k and References

No.	Reaction	Rate k ($cm^3\ s^{-1}$)	References
R1	$C_2H_2 + e \longrightarrow CH^+ + CH + 2e$	Collis. cross section	(1)
R2	$C_2H_4 + e \longrightarrow C_4H_2^+ + 2e$	Collis. cross section	(2)
R3	$C_2H_6 + e \longrightarrow C_6H_2^+ + 2e$	Collis. cross section	(2), (17)
R4	$C_2H^+ + C_2H_2 \longrightarrow C_4H_2^+ + H$	1.85×10^{-9}	(2), (3), (4), 5)
R5	$C_6H_2^+ + C_2H_2 \longrightarrow C_8H4^+$	4.3×10^{-11}	(2), (3), (4), 5)
R6	$C_6H_5^+ + C_2H_2 \longrightarrow C_8H_6^+ + H$	7.8×10^{-11}	(2), (3), (4), 5)
R7	$C_8H_6^+ + C_2H_2 \longrightarrow C_10H_6^+ + H_2$	5.0×10^{-11}	(2), (3), (4), 5)
R8	$C_10H_6^+ + C_2H_2 \longrightarrow C_12H_6^+ + H_2$	5.0×10^{-11}	(2), (3), (4), 5)
R9	$C_2H_2 + C_4H_2^+ \longrightarrow C_6H_4^+$	5.0×10^{-11}	(2), (3), (4), 5)
R10	$C_2H_2 + C_4H_3^+ \longrightarrow C_6H_5^+$	2.9×10^{-11}	(2), (3), (4), 5)
R11	$N + CH_3 \longrightarrow HCN + H_2$	1.4×10^{-11}	(2), (3), (4), 5)
R12	$N + CH_2 \longrightarrow HCN + H$	5.0×10^{-11}	(2), (3), (4), 5)
R13	$N + H_2CN \longrightarrow HCN + NH$	6.7×10^{-11}	(2), (3), (4), 5)
R14	$CN + CH_4 \longrightarrow HCN + CH_3$	2.9×10^{-11}	(2), (3), (4), 5)
R15	$CN + C_2H_6 \longrightarrow HCN + C_2H_5$	1.8×10^{-11}	(2), (3), (4), 5)
R16	$H_2CN + H \longrightarrow HCN + H_2$	2.9×10^{-11}	(2), (3), (4), 5)
R17	$N(^2D) + CH_4 \longrightarrow CH_2NH + H$	$3.84 \times 10^{-11} e^{-750/T}$	(6)
R18	$N(^2D) + CH_4 \longrightarrow NH + CH_3$	$9.6 \times 10^{-12} e^{-750/T}$	(6)
R19	$NH + CH_3 \longrightarrow CH_2NH + H$	$3.12 \times 10^{-16} T^{1.55} e^{-103/T}$	(7), (18)
R20	$CN + CH_2NH \longrightarrow H_2CNCN + H$	2.7×10^{-11}	(8), (16)
R21	$CH_5^+ + CH_2NH \longrightarrow CH_2NH_2^+ + CH_4$	3.0×10^{-9}	(6)
R22	$H + CH_2NH \longrightarrow H_2CN + H_2$	4.0×10^{-14}	(6)
R23	$NH_2 + H_2CN \longrightarrow NH_3 + HCN$	$5.42 \times 10^{-11} (T/300)^{-1.06} e^{-60.8/T}$	(6)
R24	$CH_3^+ + NH_3 \longrightarrow CH_2NH_2^+ + H_2$	1.0×10^{-9}	(9)
R25	$NH + H_2 \longrightarrow NH_3$	1.0×10^{-9}	(9)
R26	$N(^2D) + H_2 \longrightarrow NH + H$	$4.2 \times 10^{-11} e^{-880/T}$	(6)
R27	$NH_2 + H \longrightarrow NH + H_2$	5.25×10^{-12}	(10)
R28	$N_2^+ + CH_4 \longrightarrow N_2H^+ + CH_3$	3.42×10^{-11}	(11)
R29	$N_2H^+ + C_2H_2 \longrightarrow N_2 + C_2H_3^+$	1.41×10^{-9}	(13)
R30	$CH_4 + NH_2 \longrightarrow CH_3 + NH_3$	3.99×10^{-14}	(12)
R31	$C_2H_2 + NH_2 \longrightarrow C_2H + NH_3$	1.11×10^{-13}	(12)
R32	$C_2H_4 + NH_2 \longrightarrow C_2H_3 + NH_3$	3.42×10^{-14}	(12)
R33	$C_2H_5 + NH_2 \longrightarrow C_2H_4 + NH_3$	4.15×10^{-11}	(12)
R34	$C_2H_6 + NH_2 \longrightarrow C_2H_5 + NH_3$	6.14×10^{-13}	(12)
R35	$C_2H_6 + N^+ \longrightarrow NH + C_2H_5^+$	1.0×10^{-10}	(13)
R36	$C_2H_6 + N^+ \longrightarrow NH_2 + C_2H_4^+$	5.5×10^{-10}	(13)
R37	$C_2H_6 + N + \longrightarrow NH_3 + C_2H_3^+$	2.5×10^{-10}	(13)
R38	$C_2H_6 + N^+ \longrightarrow CH_4 + HCNH^+$	1.0×10^{-10}	(12)
R39	$NH + C_2H_2 \longrightarrow HC_2N + H_2$	$2.01 \times 10^{-9} T^{-1.07}$	(6), (14)
R40	$NH + C_2H_4 \longrightarrow CH_3CN + H_2$	$2.3 \times 10^{-12} (T/300)^{-1.09}$	(6), (14)
R41	$NH + C_2H_6 \longrightarrow C_2H_5N + H_2$	6.8×10^{-12}	(6), (14)
R42	$NH + C_4H_2 \longrightarrow C_4HN + H_2$	$8.24 \times 10^{-9} T^{-1.23}$	(6), (14)
R43	$CH_2NH_2^+ + e \longrightarrow CH_2NH + H$	$1.0 \times 10^{-6} (300/T_e)^{0.7}$	(6)
R44	$CH_2NH_2^+ + e \longrightarrow CH_2 + NH_2$	$1.0 \times 10^{-6} (300/T_e)^{0.7}$	(6)
R45	$N_2H^+ + e \longrightarrow NH + N$	$5.67 \times 10^{-8} (300/T_e)^{0.51}$	(9), (15), (16)

References. (1) C. Tian & C. R. Vidal (1998); (2) K. De Bleecker et al. (2006b); (3) G. Angelova et al. (2004); (4) J. Benedikt (2010); (5) S. Janalizadeh et al. (2023); (6) R. V. Yelle et al. (2010); (7) M. Rosi et al. (2018); (8) V. Barone & C. Puzzarini (2022); (9) N. Carrasco et al. (2012); (10) N. Harada et al. (2010); (11) S. Plessis et al. (2010); (12) E. Hébrard et al. (2009); (13) V. G. Anicich (2003); (14) C. Mullen & M. A. Smith (2005); (15) W. D. Geppert et al. (2004); (16) F. Vazart et al. (2015); (17) M. Mao et al. (2008); (18) J. Bourgalais et al. (2019).

pathways presently in the model are shown in Figures 2 and 3, respectively.

To assess the impact of these changes on the modeled chemistry, we then ran the updated 1D model simulations for gas mixtures listed in Table 1 (N_2–CH_4) and computed synthetic mass spectra from the calculated molecular abundances near the outlet before comparing them with the previous synthetic spectra and the experimental spectra presented in A. W. Raymond et al. (2018). We also performed a sensitivity analysis of this new version of CO-PRISM, calculating the molar concentrations of the molecular products (1) across the entire plasma channel (from inlet to outlet) to identify potential wall effects at the electrodes and (2) when changing some of the experimental parameters (voltage on the electrodes, molecular precursors; see Table 1) to assess their impact on the chemical pathways, in particular on the nitrogen chemistry in COSmIC, and how they relate to the solid phase analyses. The range of initial N_2–CH_4 mixing ratios considered

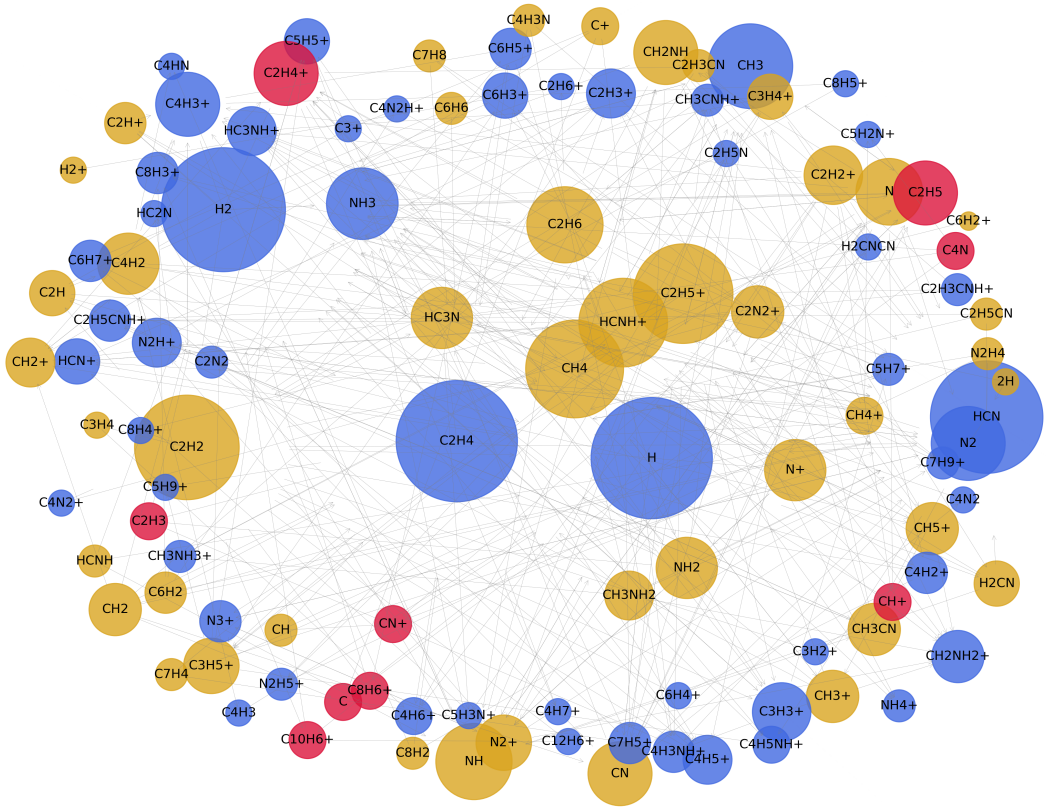

Figure 2. Schematic diagram showing all the model pathways leading to the production of both neutrals and cations. Each molecular species indicated here has a node whose size is proportional to the number of times this species is either lost or produced in the overall scheme. The larger the node, the more important that molecule's contribution to the network. In blue are species participating mainly as a formed product. In gold are species participating mainly as a reactant. Species in crimson are in reactant–product equilibrium.

falls within the typical range of methane concentrations ($\sim$1%–10% $[CH_4]_0$) usually considered in theoretical and experimental atmospheric simulations of Titan (see the Introduction).

3. Results and Discussion

3.1. Comparison of Mass Spectra

To first assess the impact of the changes applied to the reaction scheme on the calculated synthetic mass spectra, we ran the model using the same gas mixture used with the original version of CO-PRISM (A. W. Raymond et al. 2018), i.e., the N_2–CH_4 (90:10), N_2–CH_4–C_2H_2 (85:10:5), and N_2–CH_4–C_2H_4 (85:10:5) gas mixtures. We considered a gas flow of 2000 sccm, a gas temperature of 150 K, and a high voltage of -800 V in the model to match the experimental parameters. A seed electron density of $n_e = 10^7$ cm^{-3} was considered. Positive ion synthetic mass spectra were computed from the output molar fraction of all the species calculated near the cathode, i.e., close to their collection point as probed by the mass spectrometry in the experiments (E. Sciamma-O'Brien et al. 2014).

Figure 4 shows the comparison of the model spectra obtained with the original version of CO-PRISM (red diamonds) and experimental mass spectra (yellow bars) with newly calculated mass spectra (blue circles; this study) showing species ranging from *m/z* 13 up to *m/z* 79. All spectra hereafter are normalized to the intensity found at *m/z* 16 to stay consistent and comparable with the normalizations in E. Sciamma-O'Brien et al. (2014) and A. W. Raymond et al. (2018).

The updated reaction rates in the model affect the molecular abundance of the product species and result in the production of new species compared to the previous version of the model. Almost all major ions observed experimentally are reproduced by the model. The new reaction network generally exhibits a lower ion abundance compared to the previous model (red diamonds to blue circles), bring the intensities generally closer to the experimental value (e.g., *m/z* 15, 28, C5, and C6 species). Although there are still some discrepancies, the previous intensities at these masses were higher than the experimental ones.

In the simple N_2–CH_4 (90%:10%) mixing ratio, no hydrocarbons are formed above *m/z* 30; a single ion at *m/z* 42 is observed (corresponding to N_3^+). With the new version of CO-PRISM, in the N_2–CH_4 (90%:10%) gas mixture, we observe a small contribution of *m/z* 30, which we attribute to protonated methanimine ($H_2C = NH_2^+$) produced by the newly added reactions R21 and R24 (see Table 2). Protonated methanimine (and its parent molecule, methanimine) production relies on the presence of CH_3^+, CH_5^+, and neutral methanimine itself. Although the intensity is low, this represents the first measurable amount of protonated methanimine calculated in the COSmIC plasma. It was not produced in the previous version of the model. Including reaction pathways for the formation of methanimine and protonated methanimine allows for the modeling of a small contribution

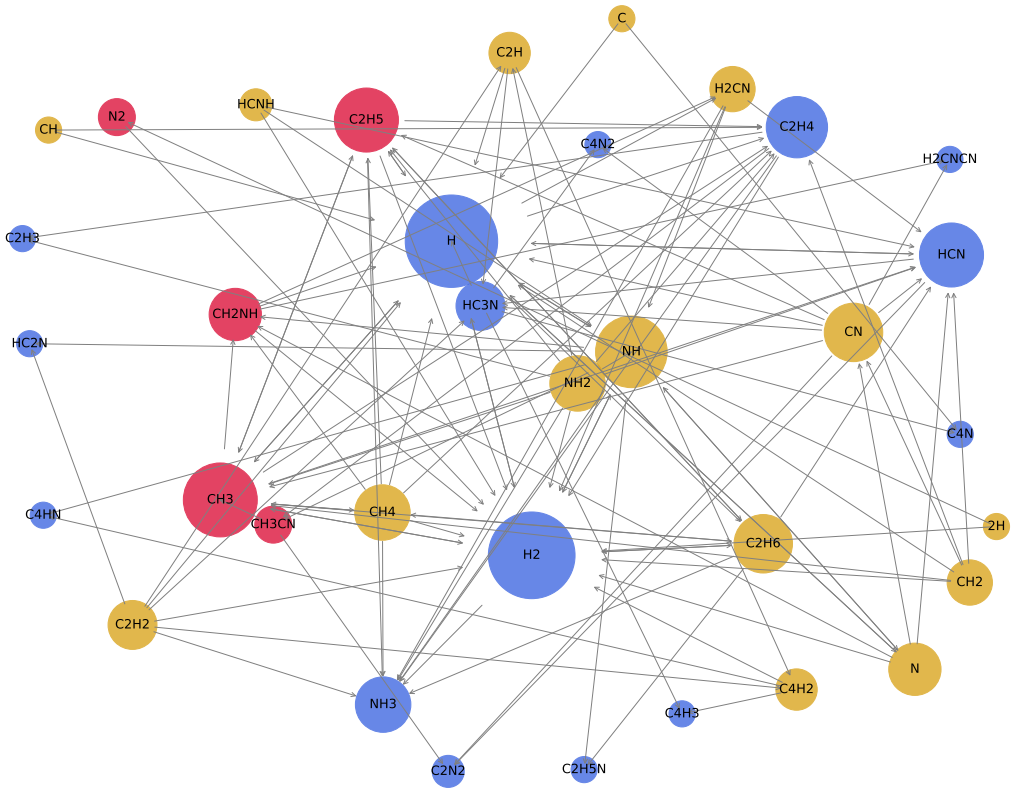

Figure 3. Schematic diagram showing the model pathways only involving neutral species in neutral–neutral reactions. The interpretation of the diagram is the same as in Figure 2.

from these molecules to the peaks observed experimentally at *m/z* 29 and *m/z* 30, respectively. The main contributor to the 29 m/z peak remains $C_2H_5^+$, with an abundance of $\sim 10^{-7}$ in the model (see Section 3.4.1). We interpret the discrepancy observed in the *m/z* 30 peak as missing chemical pathways in the CO-PRISM chemical network that would lead to the formation of protonated methanimine and ionized ethane ($C_2H_6^+$). Methanimine being a transient species, it is also possible that it is rapidly lost through barrierless reactions with other ions through unknown pathways not incorporated into our reaction scheme. At present, only three loss mechanisms are included in CO-PRISM for the loss of methanimine (Table 2): R20, R21, and R22. Other destruction pathways contributing to the loss of CH_2NH and the production of $CH_2NH_2^+$ through bimolecular reactions with $C_2H_5^+$, $C_3H_5^+$, and $C_4H_3^+$ also exist but are not included in our scheme (S. Plessis et al. 2010).

To improve the agreement between the modeled spectra and experiments involving C_2H_6 and N_2H^+ ion–neutral reactions, it may be useful to incorporate the reaction mechanisms obtained from H_2-based cold plasma discharges in I. Tanarro et al. (2007) in future work. It is also possible that methanimine is more favorably produced under direct UV/EUV irradiation conditions (J. Bourgalais et al. 2019) stemming from a favorable photolysis of N_2 by UV photons (R. V. Yelle et al. 2010). Future measurements outside of the scope of this study utilizing isotopically labeled CH_4 would confirm whether methanimine is efficiently produced in the COSmIC plasma. Such measurements would also guide future modeling analyses including additional reaction pathways leading to methanimine production. On the other hand, *m/z* 27 is observed in N_2–CH_4 experiments but is not predicted by the model. In the more complicated mixtures containing C_2H_2 and C_2H_4, however, products are observed at *m/z* 27 both experimentally and via modeling and predicted to be $C_2H_3^+$ and HCN^+. Their production is facilitated by reactions R29 and R32 in Table 2. The species NH_2 and N_2H^+ appear to be a missing link in the production of HCN^+ and $C_2H_3^+$ in the N_2–CH_4 modeling. Two main pathways currently include the production of $C_2H_3^+$ (see Reactions (21) and (137) in the Appendix), but future work should also incorporate other bimolecular reactions, such as $CH^+ + CH_4 \longrightarrow C_2H_3^+ + H_2$ (M. J. McEwan & V. G. Anicich 2007).

Adding C_2H_2 to the precursor mixtures allows the chemistry in the plasma to further evolve and results in the production of more complicated C4, C5, and C6 hydrocarbons. The revised reaction network leads to improved agreement with the experimental spectrum for the peaks at *m/z* 17, 25, 29, 39, 40, and 65. These peaks correspond mainly to CH_5^+, C_2H^+, $C_2H_5^+$, $C_3H_3^+$, $C_3H_4^+$, and $C_5H_5^+$, respectively. Reactions R1, R2, R3, and R35 all facilitate the production of these species, ions resulting from the collisional dissociation of C_2H_2, and the addition of the new collisional cross sections. We note, however, that the absence of calculated products at *m/z* 52 (contributed by $C_4H_4^+$ and HC_3NH^+) is due to limited knowledge of $C_4H_4^+$ reaction rates and minimal production of HC_3NH^+. Future inclusion of $C_4H_4^+$ production via the bimolecular reaction between N_2^+ and C_6H_6 may explain the lack of peak at *m/z* 52 (S. T. Arnold et al. 1999), although formation of $C_4H_4^+$ under low-pressure plasma conditions is expected to be marginal (P. P. Bera et al. 2015). Products at *m/z* 38 can correspond to either CNC^+ or $C_3H_2^+$, the latter being more abundant. The inclusion of new C_2H_2 pathways to the updated reaction scheme results in substantial formation of

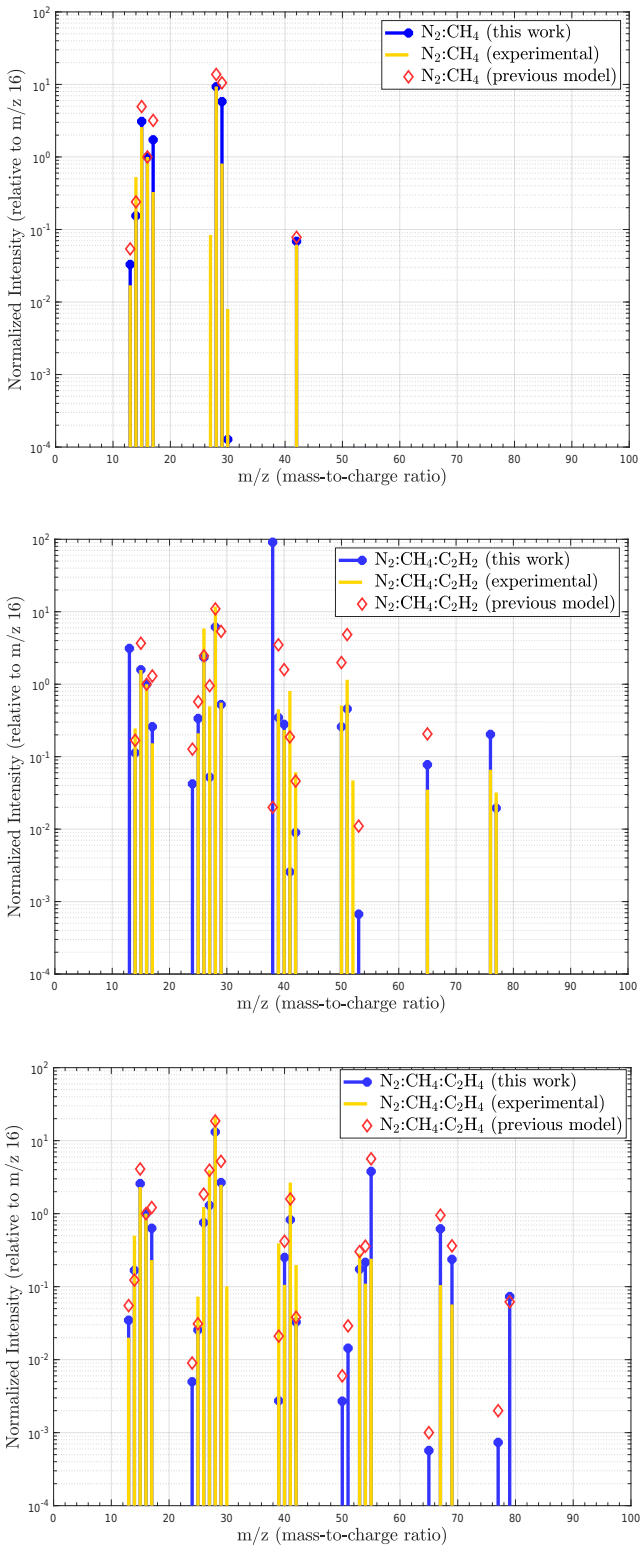

Figure 4. Comparison of the original calculated and experimental mass spectra (in red diamonds from A. W. Raymond et al. 2018 and yellow bars from E. Sciamma-O'Brien et al. 2014, respectively) with newly calculated mass spectra (in blue circles; this study) in N_2–CH_4 (90%:10%), N_2–CH_4–C_2H_2 (85%:10%:5%), and N_2–CH_4–C_2H_4 (85%:10%:5%) gas mixtures. Intensities are normalized over the intensity at *m/z* 16, and all measurements and calculations were performed with a −800 V cathode potential.

$C_3H_2^+$ at *m/z* 38 through $C_2H_2 + CH^+ \longrightarrow H + C_3H_2^+$. The discrepancy observed for this peak between the experimental and predicted peak is likely due to missing loss channels or inaccurate rates. The $C_3H_2^+ + CH_4 \longrightarrow CH_3 + C_3H_3^+$ channel may in the future fill this gap, leading to a loss of $C_3H_2^+$ (*m/z* 38) and the formation of $C_3H_3^+$ (*m/z* 39; M. J. McEwan & V. G. Anicich 2007). An improvement now observed in the model outputs, compared to the original model, is the predicted production of molecules at masses *m/z* 76 and 77 in the N_2–CH_4–C_2H_2 plasma, as observed experimentally. These peaks correspond to the benzene fragments $C_6H_4^+$ and $C_6H_5^+$, both observed in E. Sciamma-O'Brien et al. (2014; and also found to be the two most important C6 ions in a different experimental setup; D. Dubois et al. 2020). It is likely that these products could then be the starting points for larger products to be formed (E. Sciamma-O'Brien et al. 2014). Future work might incorporate pathways including even larger products and thus examine the C_2H_2 contribution further.

The mixture involving C_2H_4 is the most complex and begins to show the limitations of the modeling to describe the experiment. Overall, the C1–C3 peaks are still in good agreement; however, in blocks C4 and C5, there are bins for which the model predicts the production of species that are not observed in the experiment (*m/z* 50, 51, 65, 77, and 79). *m/z* 50 corresponds to $C_4H_2^+$, *m/z* 51 corresponds to $C_4H_3^+$, *m/z* 65 corresponds to $C_5H_5^+$, *m/z* 77 corresponds to $C_6H_5^+$, and *m/z* 79 corresponds to $C_6H_7^+$. Many of those predicted abundances are at or below the limit of the lowest-intensity experimental detections observed across any of the mixtures ($\sim 10^{-2}$). Those species may be present in the experiment but in too low a quantity to be detected. It is also possible that some reactions might be missing from our reaction scheme that would account for the loss of these species. Another possibility is that at least some of those species may contribute to the formation of solids (tholin). The loss of gas product due to solid formation is not accounted for in the model.

Adding C_2H_4 increases the population of the C5 block, dominated by $C_5H_7^+$ and $C_5H_9^+$ due to the direct loss of neutral C_2H_4 and ion $C_2H_4^+$ (A. W. Raymond et al. 2018). From the updated reaction scheme, it appears that both $C_2H_4^+$ and $HCNH^+$ should be highly sensitive to the N_2/CH_4 ratio (R1, R38, and $C_2H_4 + e \longrightarrow C_2H_4^+ + 2e$), while neutral C_2H_4 loss can readily occur through the following reaction: $N + C_2H_4 \longrightarrow C_2H_3N + H$. In addition, a shift in the C6 block is observed when adding C_2H_4 to the N_2–CH_4 plasma, with, in particular, a large increase in intensity of the *m/z* 79 peak, resulting from the protonation of benzene due to proton transfer between benzene and $C_2H_5^+/HCNH^+$ (V. Vuitton et al. 2019). The lack of any experimental detection in that region in a N_2–CH_4–C_2H_4 mixture could be due to instrument limitation, C_6H_6 limitation, loss of gas molecular products due to tholin formation, or a combination of these three possible factors. In any case, these calculations demonstrate that the presence of C_2H_2 largely influences the production of C_6H_6 and its (de)protonated derivatives.

As seen in Figure 4, for all three gas mixtures, the largest product species observed experimentally in the plasma have *m/z* of 77 and 79. The largest calculated species participating in the reaction network, however, is $C_12H_6^+$, with an *m/z* of 150. The nondetection in the experimental spectra of any species larger than *m/z* 79 when adding C_2H_4 might mean that (1) we are at the detection limit of the instrument with insufficient quantities being produced to be detected with our instrument, and/or (2) these species are solid phase precursors and are therefore lost to the solid phase, with the remaining gas

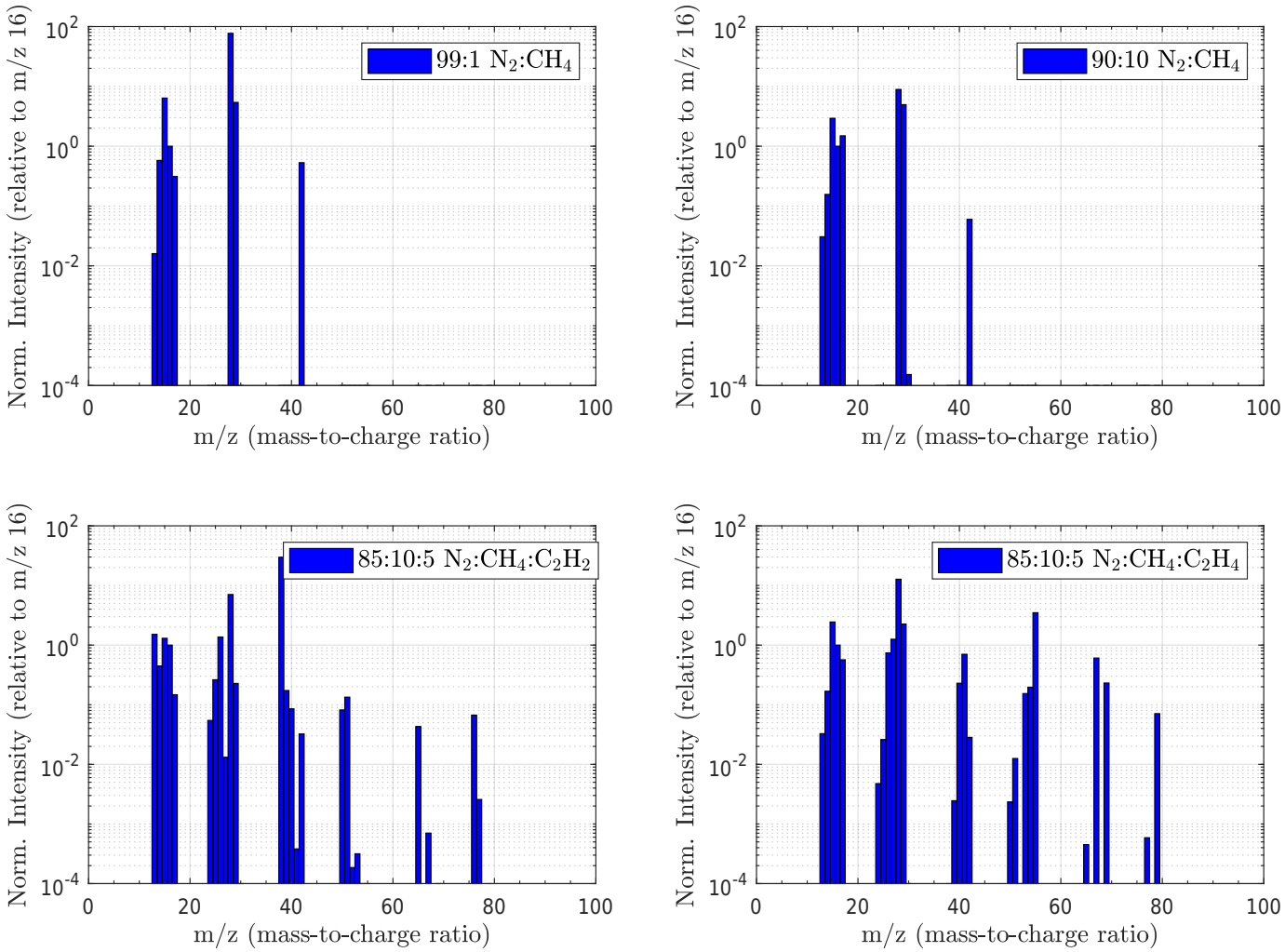

Figure 5. Mass spectra of various N_2–CH_4-based plasmas computed with 1% and 10% CH_4 and 5% C_2H_2 and C_2H_4. Intensities are normalized to the peak at $m/z = 16$.

phase abundance being too low for detection. Also, production of $C_12H_6^+$ (thanks to R8) is limited by the availability of $C_8H_6^+$ and $C_10H_6^+$ (R6 and R7). E. Sciamma-O'Brien et al. (2014) demonstrated that larger compounds could be detected experimentally when benzene was present in the initial gas mixture, which would be interesting to investigate in future modeling studies.

3.2. Calculated Mass Spectra in Other Nitrogen- and Hydrocarbon-based Conditions

In addition to conducting the comparative study with COPRISM run with plasma parameters (voltage, gas mixtures) similar to those used in the A. W. Raymond et al. (2018) study, we also modeled plasmas operated with an applied voltage of −1000 V for various gas mixtures. N_2–CH_4 (90–10) and N_2–CH_4–C_2H_2 (85–10–5) gas mixtures were first chosen to be consistent with two recent solid phase studies conducted with COSmIC (M. Nuevo et al. 2022; E. Sciamma-O'Brien et al. 2023), where the elemental composition and optical properties of the solids and the impact of the plasma parameters were investigated. We then expanded the range of plasma parameters by modeling additional gas mixtures in a −1000 V plasma, such as N_2–CH_4 (99–1), N_2–CH_4–C_2H_4 (85–10–5), N_2–CH_4–C_2H_6 (85–10–5), N_2–CH_4–NH_3 (85–10–5), N_2 – CH_4 – HCN (85–10–5), and N_2–CH_4–CH_2NH (85–10–5), to see the effect of the molecular precursors on the chemistry.

Figure 5 shows the calculated mass spectra obtained with the model for the two N_2–CH_4 mixtures, as well as the N_2–CH_4–C_2H_2 and N_2–CH_4–C_2H_4 mixtures. The calculated mass spectra for the other mixtures are provided in the Appendix, in Figure 13. When comparing the N_2–CH_4 (99%:1%) plasma model to the N_2–CH_4 (90%:10%) plasma model, we note an increase in CH_3^+ at *m/z* 15 and CH_5^+ at *m/z* 17 in N_2–CH_4 (99%:1%), as well as an absence of any protonated methanimine CH_3N at *m/z* 30. In spite of a lower amount of CH_4 available in the 99%:1% mixture, CH_3^+ production remains important through Reaction (12) (C. D. Pintassilgo et al. 1999):

$$CH_4 + N_2(X) + \longrightarrow N_2(X) + H + CH_3^+. \quad (12)$$

Other peaks show very small variations (<5%) between the two mixtures. The overall aspects of the calculated mass spectra for the N_2–CH_4–C_2H_2 and N_2–CH_4–C_2H_4 modeled plasma at −1000 V are similar to those obtained at −800 V with no significant changes observed by increasing the voltage. For the other four N_2–CH_4-based mixtures containing C_2H_6,

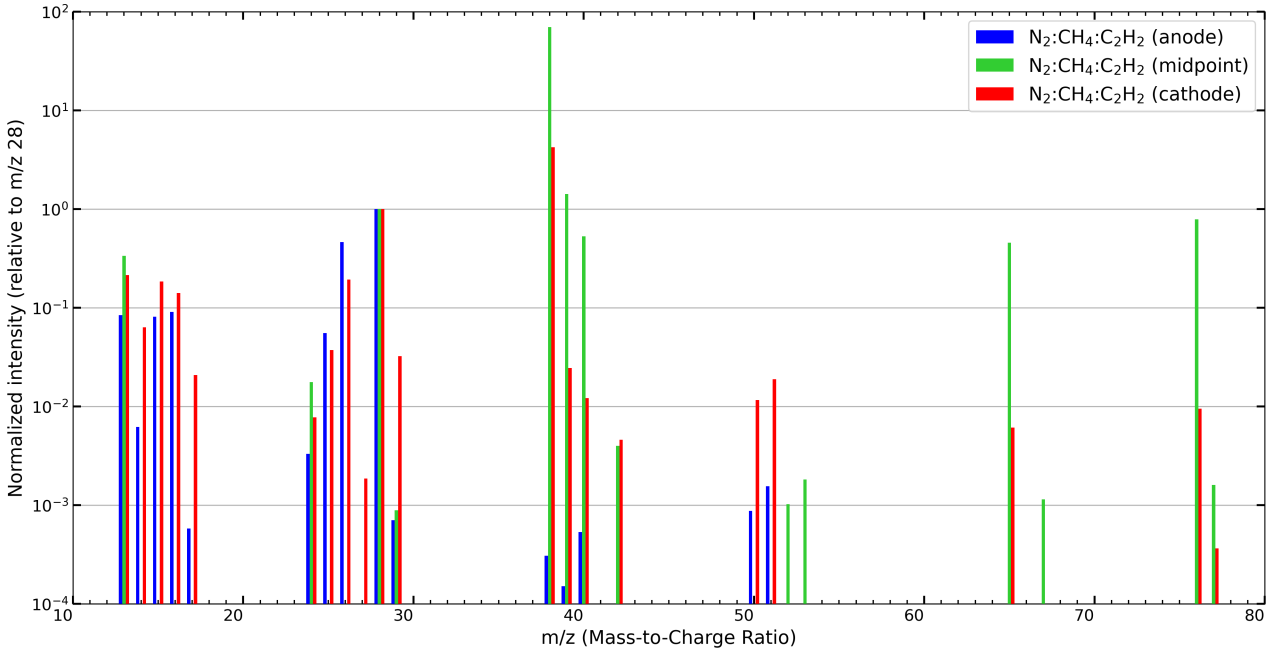

Figure 6. Mass spectra of a modeled plasma generated in a N_2–CH_4–C_2H_2 (85%:10%:5%) gas mixture with the updated version of CO-PRISM at three different locations in the plasma channel: $x = 0.004$ mm (blue; anode), $x = 0.075$ mm (green; midpoint), and $x = 1.496$ mm (red; cathode). Peaks are normalized by the intensity at *m/z* 28.

NH_3, HCN, and CH_2NH, the calculated mass spectra appear identical to N_2–CH_4 (90%:10%; Figure 13 in the Appendix).

3.3. Sensitivity Analysis Along the Plasma Cavity

In addition to conducting a comparative analysis between the original and updated version of CO-PRISM for N_2–CH_4-based plasmas produced in COSmIC, we also conducted a parameter space study to expand on our previous work (A. W. Raymond et al. 2018) and assess the sensitivity of the model on the resulting plasma chemistry when looking at different locations in the plasma channel and when changing the plasma conditions (e.g., different potentials) and the precursor gas composition (e.g., different concentrations of CH_4 in N_2 and addition of other minor species). Understanding the impact of the plasma parameters allows us to optimize the experiment for Titan simulations.

3.3.1. Plasma Chemistry Along the Plasma Channel

We recalculated the mass spectra of a simulated N_2–CH_4 (90:10) plasma discharge in COSmIC at the plasma channel edge ($x = 1.496$ mm) and also at upstream locations: $x = 0.750$ mm (midpoint) and $x = 0.004$ mm (near anode). The spectra for a N_2–CH_4–C_2H_2 (85:10:5) plasma at -1000 V (Figure 6) show primary methane ions near the anode, with C_2^+, C_2H^+, and $C_2H_2^+$. Small amounts ($<10^{-3}$) of $C_2H_5^+/N_2H^+/N_3^+$ appear. Midpoint products like $C_3H_2^+$ at *m/z* 38 reach high intensities, indicating significant methane consumption essential for chemical growth. Benzene products at *m/z* 76 and 77 emerge as $C_6H_4^+$ becomes abundant. Near the cathode, C1 and C2 species rebound, while C3 decreases notably. C4 species appear, and C5 and C6 species drop significantly, highlighting their role as intermediates in forming larger organics and aerosols, evidenced by the changes observed between the midpoint and cathode regions.

3.3.2. Electron Density as a Function of Voltage, Time, and Position in the Plasma Channel

Electron density is a crucial plasma parameter, influencing reaction schemes, electron energy distribution, collision frequency, and degree of ionization (S. Stoykov et al. 2001; K. De Bleecker et al. 2006a, 2006b; M. Mao et al. 2008; A. W. Raymond et al. 2018). We calculated electron density profiles along the plasma channel from anode to cathode for seven gas mixtures (Table 1) at a cathode potential of -1000 V. The profiles, shown in Figure 7(a), are categorized into three classes: low density (peak $<10^{18}\,m^{-3}$), intermediate density (peak $\sim 2 \times 10^{18}\,m^{-3}$), and high density (peak $>10^{20}\,m^{-3}$). Low electron density distributions are observed in N_2–CH_4, N_2–CH_4–C_2H_6, N_2–CH_4–HCN, and N_2–CH_4–CH_2N plasmas, with similar overall profiles. Intermediate electron density is seen in N_2–CH_4–C_2H_4 plasmas, while the highest density is found in N_2–CH_4–C_2H_2 plasmas, attributed to the release of twice as many electrons upon C_2H_2 dissociation (R1 and Appendix Table A1). Near the cathode, a drop in electron density indicates a larger Debye length, consistent with reduced shielding (J. R. M. Remy et al. 2003; B. H. Broks et al. 2005a; B. H. P. Broks et al. 2005b). Drops in electron density near the anode and cathode highlight sheath regions where electrons are accelerated, with the anode's dark space being thinner due to pressure differences (J. R. M. Remy et al. 2003). Near the anode, the micrometer-range mean free path results in a nearly collisionless sheath. Within the cathode's Crookes dark space, electrons are repelled by the negative potential, causing a significant drop in electric potential and electron density (B. H. P. Broks et al. 2005b).

We also calculated the electron density profiles at two given positions (near the anode and near the cathode) as a function of time to observe the different phases leading to the establishment of the steady state. Figure 7(b) shows the different phases of the electron density profile from the beginning of the plasma

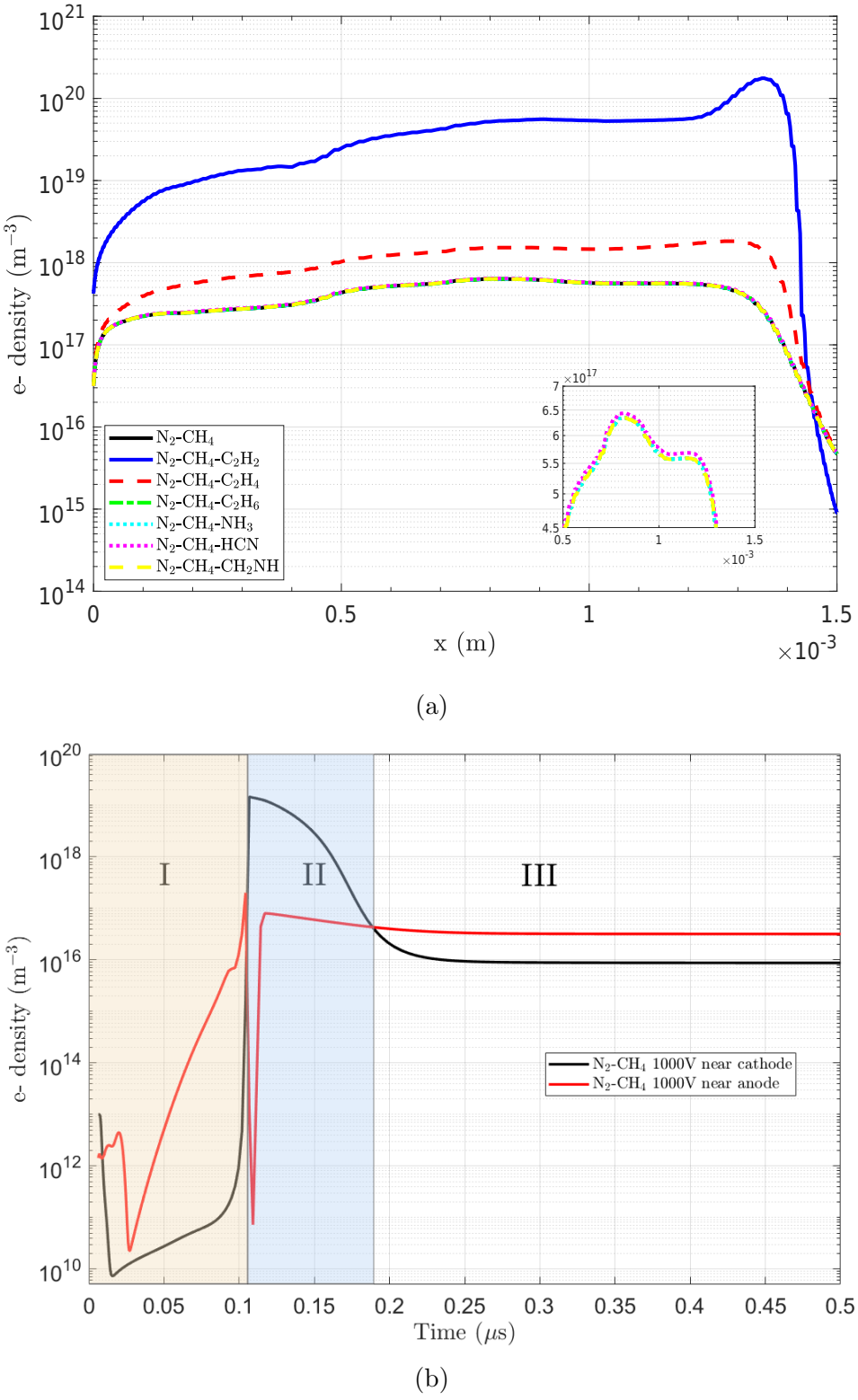

Figure 7. (a) Electron density profiles calculated along the plasma channel in seven different mixing ratio conditions. The origin coordinate, $x = 0$ mm, starts at the anode (see Figure 1). The inset shows a zoom on the lower five similar curves. (b) Electron density profiles near the anode and near the cathode calculated as a function of time during one plasma pulse, showing that the electron density steady-state conditions are reached around 0.25 μs. Phase I near breakdown shows the migration of electrons toward the anode in the first 0.1 μs. Phase II starts once a maximum density of $\sim 1.5 \times 10^{19}$ is reached with a migration of electrons to the cathode until steady-state conditions are reached around 0.25 μs (phase III).

pulse to steady-state conditions for a N_2–CH_4 (90–10) plasma discharge at −1000 V. As described in A. W. Raymond et al. (2018), at the start of the discharge (phase I; highlighted in yellow), the negative cathode voltage (black curve) increases, which results in an electron migration toward the anode (red curve) near breakdown, up to ∼0.1 μs after the start of the pulse. During this period, the electron density increases by more than 6 orders of magnitude near the anode and 2 orders

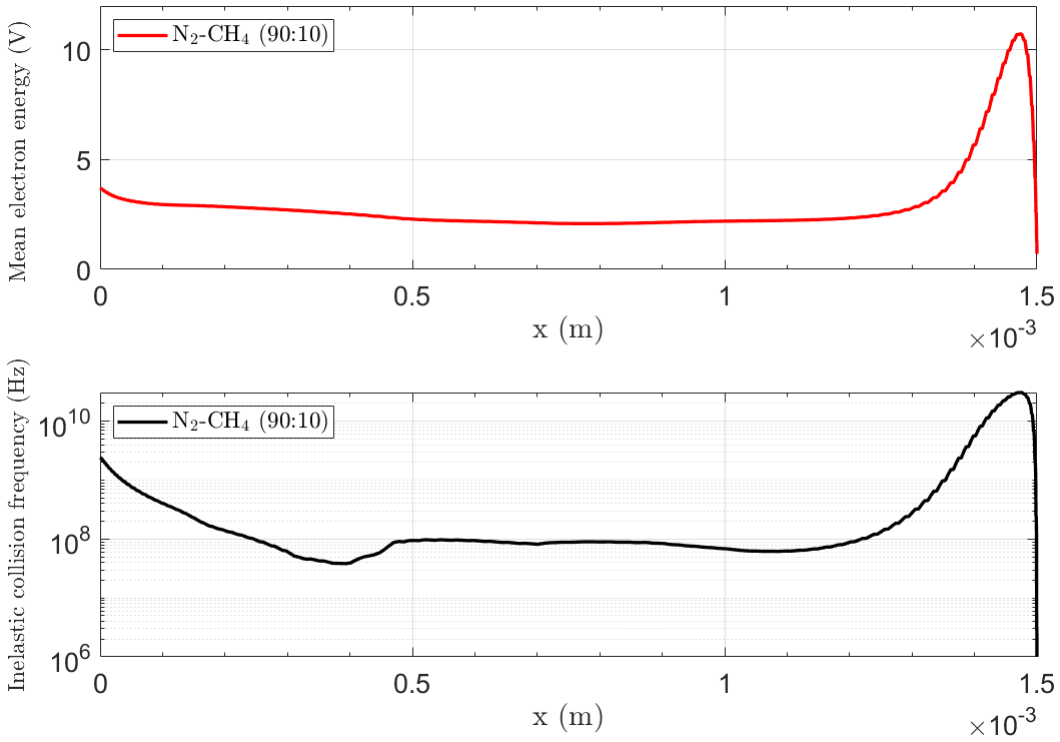

Figure 8. Top: mean electron energies (or temperatures) in eV calculated across the plasma channel for a N_2–CH_4 (90:10) plasma discharge (red). The origin coordinate starts at $x = 0$ mm (see Figure 1). Bottom: inelastic electron collision frequency across the plasma channel calculated in steady-state conditions with a source voltage of −1000 V (black). Inelastic collisions (source term S_e; see Equation (6)) lead to direct ionization and excitation of neutrals.

of magnitude near the cathode. At 0.1 μs after the start of the pulse, the electron density near the cathode reaches a peak value of 1.5×10^{19} m^{-3}. An electron density inversion and the second electron migration phase begin near 0.1 μs, this time toward the cathode (phase II; highlighted in blue), before reaching equilibrium (steady-state conditions) by 0.25 μs, where the near-anode electron density dominates again (phase III) during the steady state.

The dynamics and inversions observed here are linked to electron mobility in the plasma region and the relationship between the glow region and sheaths (J. R. M. Remy et al. 2003). The mean free path of neutrals and electrons is much larger near the cathode (mm) than near the anode (μm). This implies that electrons can enter the plasma region with high relative velocities. In the plasma, they lose their kinetic energy through collision, forming the first positive ions in the glow region. Note that given the low degree of ionization and electron density in the COSmIC plasma discharge, due to its abnormal glow nature (see J. R. M. Remy et al. 2003), electron–electron collisions are outnumbered by inelastic collisions between the carried neutral gas and electrons (B. H. P. Broks et al. 2005b).

3.3.3. Electron Energy and Inelastic Collision Frequency

As described in Equation (6), S_e is the energy source term for inelastic collisions, accounting for ionization and excitation between the electrodes. In the plasma region between the anode and cathode, trapped, runaway, and secondary electrons ionize N_2 and CH_4 neutrals. Secondary electrons are produced at a rate characterized by the secondary emission coefficient (0.025), and electron–electron collisions are not considered. Inelastic collisions, which depend on gas composition and pressure, are responsible for the direct ionization and excitation of neutrals. The bottom panel of Figure 8 shows the steady-state inelastic collision frequency in a N_2–CH_4 (90–10) gas mixture with a source voltage of −1000 V. The inelastic collision frequency is relatively steady from the anode to the plasma center (10^8–10^9 Hz) but increases sharply near the cathode by over 2 orders of magnitude to 10^{10} Hz due to high-velocity electrons causing more collisions, ions, and secondary electron generation. The top panel of Figure 8 shows the mean electron energy, which peaks at 10–11 eV near the cathode, consistent with previous Ar plasma modeling. This energy is sufficient for N_2 direct dissociation (requiring >9.76 eV) and electron impact ionization. The ionization fraction in a N_2–CH_4 plasma discharge on COSmIC (10^{-8}–10^{-5}) is comparable to Titan's upper atmosphere (10^{-7}–10^{-5}; J. R. M. Remy et al. 2003; B. H. P. Broks et al. 2005b; O. Dutuit et al. 2013; A. W. Raymond et al. 2018).

3.3.4. Positive Ion Density

Figure 9 shows the calculated total neutral and positive ion density profiles calculated at steady state in a N_2–CH_4 (90–10) gas mixture with a source voltage of −1000 V. The total neutral density is relatively constant on the order of 10^{24} m^{-3} across the plasma channel. The total positive ion density, about 6 orders of magnitude lower, reaches $\sim 6 \times 10^{17}$m^{-3} in the plasma cavity near the cathode ($x = 1.496$), which is at least 1 order of magnitude higher than the electron density at that location and on the same order of magnitude as the electron density calculated at midpoint in the plasma cavity. Given the electron and positive ion densities near the cathode, it is expected that electron impact ionization rates are on the same

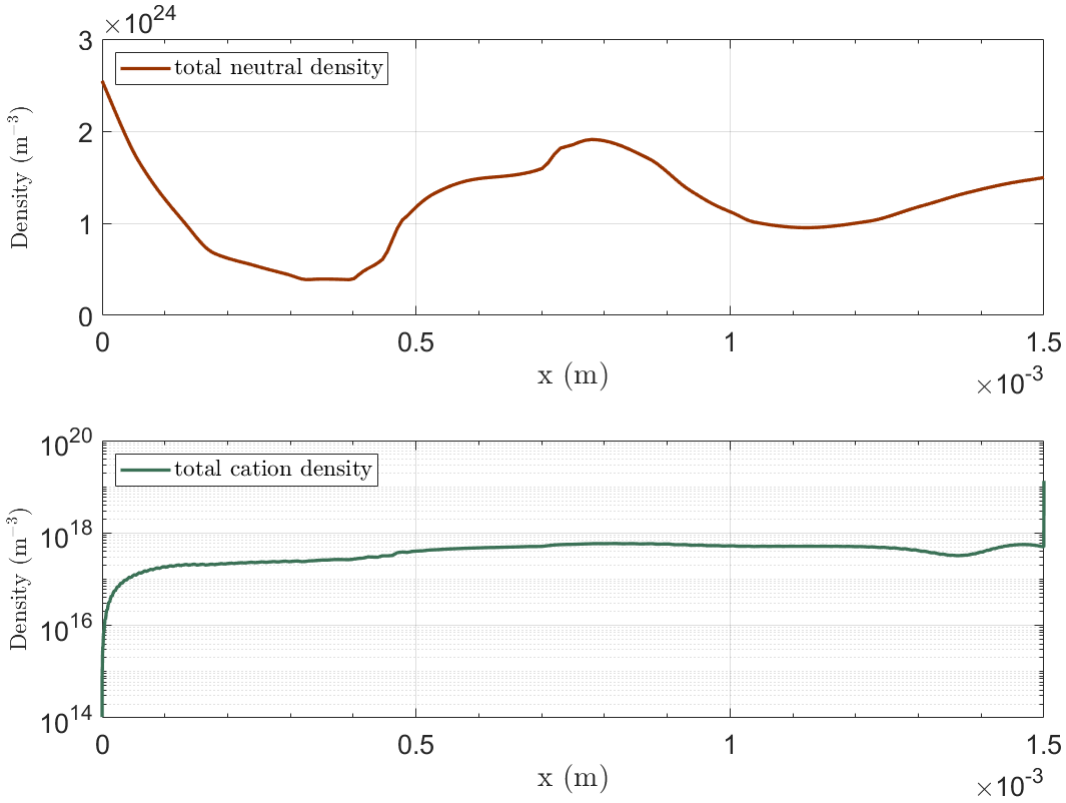

Figure 9. Total neutral and positive ion density profiles calculated in a N_2–CH_4 (90–10) gas mixture with a −1000 V source voltage.

order of magnitude as ion neutralization in this region (A. W. Raymond et al. 2018). Closer to the anode, however, the positive ion density is calculated to be several orders of magnitude lower comparatively, as the positive ions do not migrate as much upstream toward the anode. Quasi-neutrality is relatively constant throughout the plasma channel. As positive ions are formed in the plasma region, the products are then carried into the ion–neutral network, where they will be incorporated with breakdown-induced ions and neutrals. It is thus important to characterize the molecular species and plasma parameters, since these will be dependent upon the initial Titan-relevant gas mixture to be studied.

3.4. Impact of Initial Gas Mixture Composition on the Gas Phase Products

3.4.1. Light-mass Hydrocarbon Molar Fractions

As shown in Figure 5, adding heavier hydrocarbon precursors such as C_2H_2 or C_2H_4 has an impact on the chemistry and results in changes in the production yield of ion species in the modeled spectra. The addition of C_2H_2 has also been proven to have a large impact on the elemental composition of the Titan aerosol analogs (or tholins) formed in the COSmIC plasma experiments (M. Nuevo et al. 2022). In the study presented here, the impact of C_2H_2 on the plasma chemistry leading to the production of tholins was assessed by comparing the calculated molar fractions of several light-mass hydrocarbons at a steady state for modeled plasmas generated in initial N_2–CH_4 gas mixtures with and without C_2H_2. These include the following cations: CH^+, CH_3^+, $C_2H_3^+$, $C_2H_5^+$, $C_4H_3^+$, and $C_5H_5^+$. In the modeled N_2–CH_4 plasma (Figure 10(a)), $C_4H_3^+$ and $C_5H_5^+$ show the lowest predicted abundances ($\sim 10^{-28}$), while $C_2H_5^+$ reaches the highest concentration ($\sim 10^{-7}$ or on the order of 0.1 ppm), which is consistent with the relative intensities seen in the experimental mass spectrum (Figure 4). The overall profile of these species remains relatively constant throughout the plasma channel, indicating little perturbance by chemistry other than the limited migration of ions near the anode, as discussed above. This also suggests that in N_2–CH_4 plasmas, the main engine of hydrocarbon growth is driven by a handful of cations such as $C_2H_3^+$ and $C_2H_5^+$. $C_2H_5^+$ in particular appears to be in excess in the model compared to experimental measurements (see Figure 4), which likely suggests that there are still missing reactions to account for the observed discrepancies. Moreover, due to the truncated nature of the pulsed plasma discharge and our reaction scheme, $C_2H_5^+$ production is facilitated over that of HCN, with which it reacts to produce $HCNH^+$ (A. W. Raymond et al. 2018). As a result, radical-induced growth of C2 and C3 species may be accentuated (J. Benedikt 2010; A. W. Raymond et al. 2018).

First we observe that $C_5H_5^+$ (formed primarily through the channel $C_2H_2 + C_3H_5^+ \longrightarrow H_2 + C_5H_5^+$) becomes the most abundant species reaching $\sim 10^{-7}$ (or on the order of 0.1 ppm) in the middle of the plasma cavity, at $x = 0.75$ mm. CH^+ is also heavily produced with a molar fraction also around 0.1 ppm at $x = 0.75$ mm and reaching almost 10 ppm closer to the cathode and back down to 0.1 ppm at the outlet of the plasma cavity. This value is higher than the CH^+ concentration of ∼0.01 ppm at the outlet of the plasma cavity obtained by A. W. Raymond et al. (2018). This difference is explained by the fact that A. W. Raymond et al. (2018) modeled a N_2–CH_4–C_2H_2 plasma with a −800 V voltage, while in our calculation, we used a higher voltage of −1000 V. Close to the

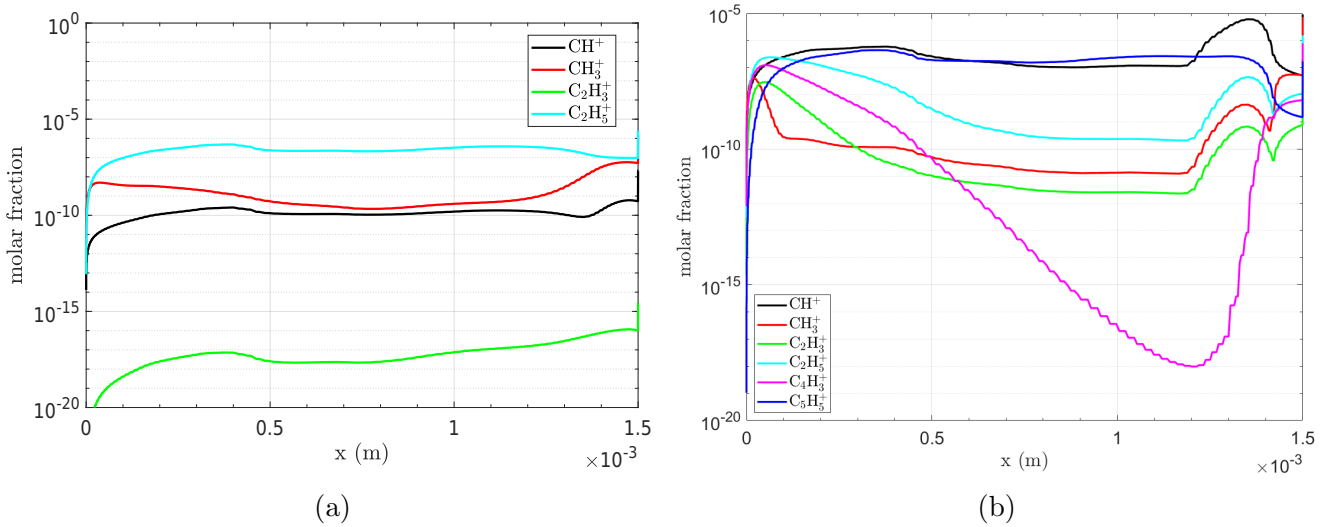

Figure 10. (a) Steady-state molar fraction profiles along the plasma channel of CH^+, CH_3^+, $C_2H_3^+$, and $C_2H_5^+$ calculated in a N_2–CH_4 (90–10) plasma with a −1000 V voltage. The molar fractions of $C_4H_3^+$ and $C_5H_5^+$ were also calculated, but their values were below 10^{-20}, which is considered to be the physical threshold. (b) Molar fraction profiles of the same molecules, including $C_4H_3^+$ and $C_5H_5^+$, have values above the physical threshold this time, calculated in a N_2–CH_4–C_2H_2 (85–10–5) plasma with −1000 V voltage. Values approaching a mole fraction of 10^{-20} represent the lower limit of what is physically possible inside the volume of the plasma cavity. Lower values close to 10^{-20} approach what is physically possible in terms of mole fraction; they are shown here for comparison purposes between the multiple species.

cathode, at $x = 1.3$–1.4 mm, we observe a sudden sharp increase in molar fractions for several species: CH^+, CH_3^+, $C_2H_3^+$, and $C_2H_5^+$. This can be explained by an increase in inelastic collision occurring in that region, specifically two channels producing $C_2H_2^+$ and free electrons:

$$e + C_2H_2 \longrightarrow C_2H_2^+ + 2e \tag{13}$$

and

$$e + C_2H_4 \longrightarrow H_2 + C_2H_2^+ + 2e. \tag{14}$$

An increase in the electron density is also observed in this region (Figure 7(a)). The higher concentration of reactive electrons, radicals, and ionic species in this region could result in higher tholin growth rates following the formation of larger molecular species, particularly through a cationic pathway (Reaction (15), after multiple acetylene or ethylene additions) recently proposed by S. Janalizadeh et al. (2023),

$$C_{2n}H_{2m}{}^+ + C_2H_2 \longrightarrow C_{2n+2}H_{2m+2}{}^+ + xH_2, \tag{15}$$

where $n = 1$–5, $x = 0$ or 1. A drastic consumption of $C_4H_3^+$ (magenta; Figure 10(b)) is also observed, which begins early on in the plasma cavity until it increases again near the cathode, at $x < 1.3$ mm. As soon as $C_4H_3^+$ is formed near the cathode, it is quickly consumed through reactions with the much more abundant C_2H_2 and C_2H_4 molecules to form the larger cations $C_6H_3^+$ and $C_6H_5^+$ (Reactions (16) and (17)). This step is expected to be a key transition toward the formation of the first C6 compounds (R. Peverati et al. 2016; A. W. Raymond et al. 2018; V. Vuitton et al. 2019):

$$C_4H_2 + C_4H_3^+ \longrightarrow C_2H_2 + C_6H_3^+, \tag{16}$$

$$C_2H_2 + C_4H_3^+ \longrightarrow C_6H_5^+. \tag{17}$$

The observed sensitivity of the plasma products, and thus the entire network, on the presence of C_2H_2 shows intrinsic evolutions that depend on the precursor gas density profile, electron mobility, and collisional efficiency. These trends can also be visualized as a function of time, as shown in Figure 11, where the molar fractions are represented in 3D as a function of time and position in the plasma cavity. CH^+ and $C_5H_5^+$ abundances do not vary as much once the electron steady-state plateau is reached, whereas CH_3^+, $C_2H_3^+$, $C_4H_3^+$, and, to a lesser extent, $C_2H_5^+$ go through a much more dynamical range of concentrations. $C_2H_3^+$ and $C_4H_3^+$ undergo an important production phase early in the plasma pulse (red increase) before being consumed (blue dips). On the other hand, $C_5H_5^+$ remains relatively stable across the pulse duration. Note that these trends do not include loss effects due to the formation of much larger molecular products such as polycyclic aromatic compounds and solid particles (tholins), as they are not included in CO-PRISM.

3.4.2. C_2H_2 and HC_3N Ionization and Mechanisms toward the Formation of Benzonitrile in a N_2–CH_4–C_2H_2 Plasma

C_2H_2 and acetonitrile (HC_3N) are both important molecules produced and detected in a variety of planetary atmospheres, molecular clouds, and star-forming regions (e.g., C. Freeman et al. 1978; R. L. Snell et al. 1981; N. A. Teanby et al. 2006; P. B. Rimmer et al. 2021). HC_3N is a simple linear molecule that possesses two triple-bonded carbons, one of them with a terminal nitrile function. It has been found to play an important role in the formation of prebiotic molecules on Earth and in the interstellar medium (ISM; L. E. Orgel 2002; D. J. Ritson et al. 2022), along with other nitriles such as HCN (M. Ferus et al. 2017; T. Stein et al. 2020) and azole compounds as an intermediate for nucleotide and amino acid synthesis (R. Shapiro 1999; D. J. Ritson et al. 2022). More recently, HC_3N (and its association with C_2H_2) was found to be an intermediate candidate in the preliminary stages of aromatic molecules formed in the ISM (J. Jose et al. 2021), particularly in the formation of benzonitrile C_7H_5N. Computationally, J. Jose et al. (2021) showed that ionized Van der Waals clusters

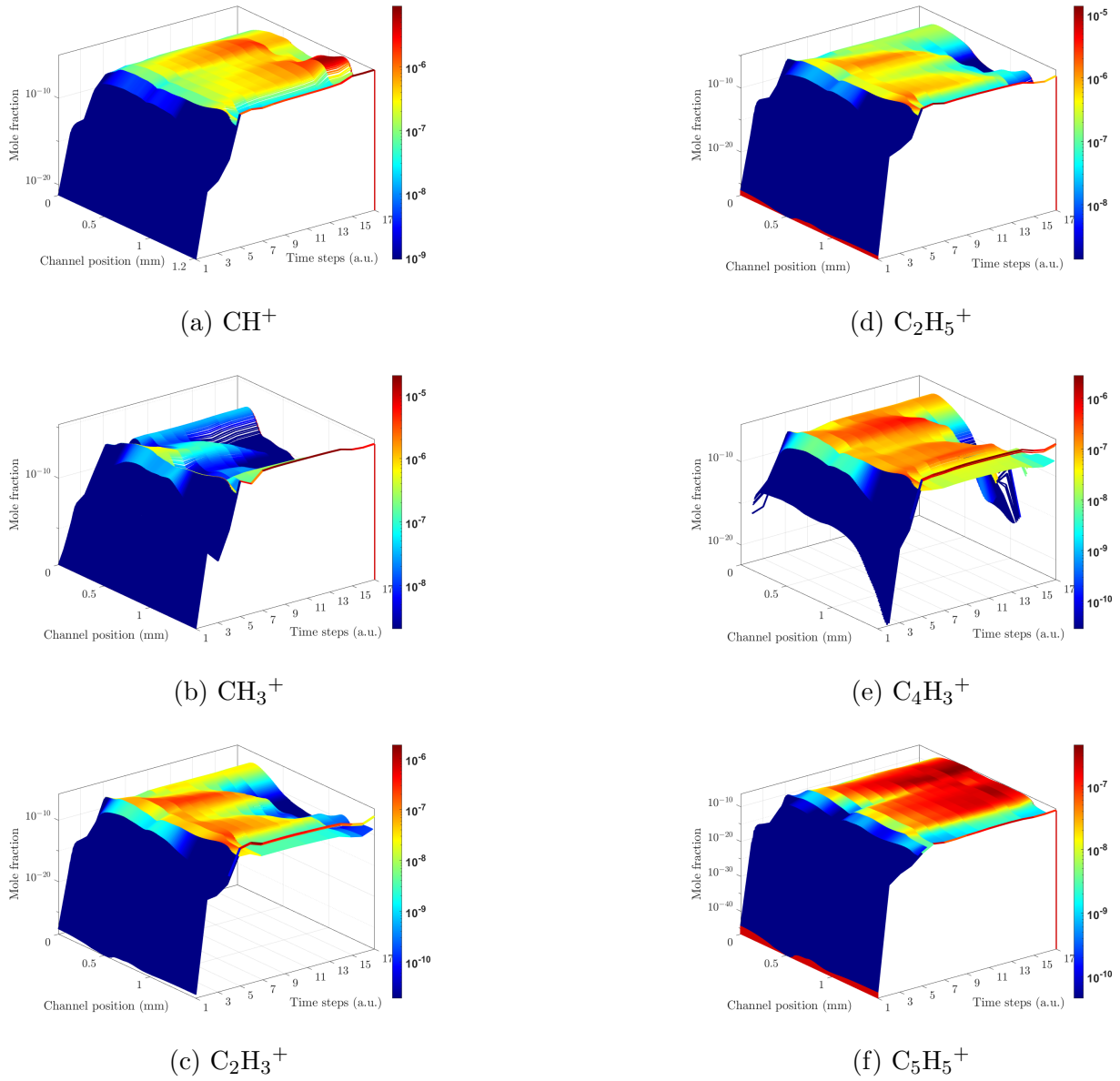

(a) CH^+ (d) $C_2H_5^+$

(b) CH_3^+ (e) $C_4H_3^+$

(c) $C_2H_3^+$ (f) $C_5H_5^+$

Figure 11. The 3D representations of the molar fractions of each cation and its time dependency calculated during one plasma pulse. The *x*-axis represents arbitrary time steps chosen from the beginning of each simulation ($t = 1$) until steady-state conditions are reached by $t = 17$. The *y*-axis is the channel distance along the plasma channel (in millimeters, where $x = 0$ mm is the anode), and the *z*-axis is the color-coded molar fraction.

containing C_2H_2 and HC_3N could lead to the formation of ISM-relevant molecules, in particular, benzonitrile. In the ionization process, an important ion, $C_5H_3N^+$, is formed through C_2H_2 and HC_3N bonding. This alyphatic ion can then serve as a backbone of larger (>C5) linear or cyclic molecules and was listed as one of the most abundant C5 candidate species in the ion–neutral reaction network by N. Carrasco et al. (2008). This highlights the potential role of C_2H_2 and HC_3N (and the intermediate ions) as crucial precursors to Titan's complex organic products. In our model, Reaction (18) follows a modified Arrhenius expression with the reaction rate $k = 2 \times 10^{-12}$ cm^3 s^{-1} (A. W. Raymond et al. 2018):

$$HC_3N + C_2H_2^+ \longrightarrow C_5H_3N^+. \quad (18)$$

In steady-state regime with a N_2–CH_4–C_2H_2 mixture, we find a maximum $C_5H_3N^+$ mole fraction of 10^{-21} near the cathode, as opposed to $\sim 10^{-46}$ at the same location in N_2–CH_4 without acetylene. This difference of 25 orders of magnitude is particularly appreciable since the initial concentration of C_2H_2 is only 5%. It shows that $C_5H_3N^+$ is sensitive to the initial concentration of C_2H_2, which also controls the production of cyanoacetylene via

$$C_2H_2 + CN \longrightarrow H + HC_3N \quad (19)$$

with a rate $k = 2.7 \times 10^{-10}$ cm^3 s^{-1} (V. Wakelam et al. 2012). Thus, in addition to C_2H_2 acting as an important precursor to double- and triple-bonded (C = C, C = N, and C ≡ N) species, it also favors the gas phase formation of tholin precursors with nitrile groups attached to aromatic species. The increase in ions such as $C_5H_3N^+$ may thus support their role as an important gas phase precursor of aromatic and unsaturated characters. Future work may be able to assess whether species like benzonitrile may be favorably formed in N_2–CH_4-based plasmas or not (V. Esposito et al. 2025).

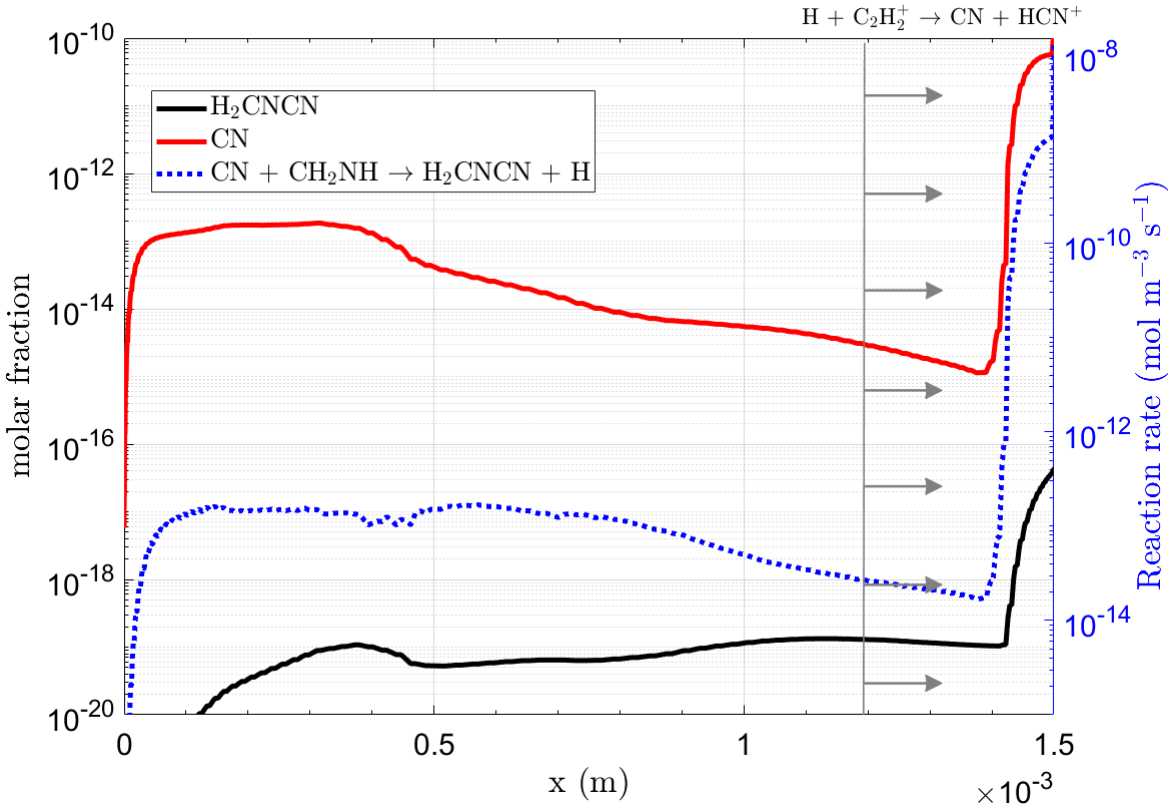

Figure 12. Calculated molar fractions for H_2CNCN (black) and CN (red) in a N_2–CH_4–C_2H_2 (85–5–5) plasma with −1000 V voltage. The reaction rate of the main reaction incorporated into our model producing H_2CNCN is also shown (dotted blue line).

3.4.3. Nitrogenated Products and Incorporation of N-bearing Ions: Formation of the Stable HCN Dimer H_2CNCN and Role of CH_2NH

If we further examine the implications for N-rich chemistry, H_2CNCN, known as cyanomethanimine, is an inorganic compound of relevant interest. It consists of a carbon–nitrogen framework where the central carbon is bonded to both an amine group (NH_2) and a nitrile group (CN). This structure gives cyanomethanimine both nucleophilic and electrophilic properties, allowing it to react in a variety of ways. It is commonly used in the synthesis of various organic compounds, including imidazoles and other nitrogen-containing heterocycles. Cyanomethanimine can also undergo hydrolysis to form ammonia and formic acid under acidic conditions. H_2CNCN has recently gained astrochemical interest since its detection in the Galactic center (D. San Andrés et al. 2024) and spectroscopic properties and formation pathways subsequently studied (R. C. Fortenberry & V. J. Esposito 2024). While condensed phase pathways are being investigated (R. C. Fortenberry & V. J. Esposito 2024), gas phase pathways (Table 2, R20) have so far (F. Vazart et al. 2015) been constrained to the following pathway:

$$CN + CH_2NH \longrightarrow H_2CNCN + H. \quad (20)$$

Although this neutral pathway remains elusive in that it cannot reproduce the recent observations of H_2CNCN (D. San Andrés et al. 2024), a putative approach was considered here to assess whether this HCN dimer may be formed under a C_2H_2/CN-enriched, Titan-like gas mixture. Figure 12 shows the H_2CNCN abundance calculated using Equation (20) and a rate $k = 2.7 \times 10^{-11}$ cm^3 s^{-1} with CO-PRISM for a N_2–CH_4–C_2H_2 modeled plasma with −1000 V voltage. H_2CNCN (black line) reaches a molar fraction ranging from $\sim 10^{-19}$ to $\sim 10^{-16}$ (or 10^{-10}–10^{-7} ppb). While these values are extremely small, they highlight the important role C_2H_2 (and $C_2H_2^+$) can play in the catalysis of nitrogen-rich molecules, according to any of the following pathways:

$$C_2H_2 + CN \longrightarrow HC_3N + H, \quad (21)$$

$$HC_3N + C_2H_2^+ \longrightarrow C_5H_3N^+, \quad (22)$$

$$N(S) + C_2H_2^+ \longrightarrow HCN + CH^+, \quad (23)$$

where $k_{21} = (2.71 \times 10^{-9}\,\mathrm{cm^3\,s^{-1}}) \cdot (T/1[\mathrm{K}])^{-0.52}\exp[-20[\mathrm{K}]/T]$, $k_{22} = (2.0 \times 10^{-12}\,\mathrm{cm^3\ s^{-1}}) \cdot (T/300[\mathrm{K}])^{-0.25}$, and $k_{23} = 2.5 \times 10^{-11}$, respectively (V. Wakelam et al. 2012). Along with acetylene, the radical CN (molar fraction shown in red) also contributes to this scheme by reacting with methanimine CH_2NH, reaching nonnegligible amounts of ∼0.1 ppm. C_2H_2, CN, and CH_2NH (formed from R17; Table 2) all contribute to the formation of H_2CNCN. In Figure 12, the temperature-dependent reaction rate for Equation (20) is shown in blue. The vertical bar and arrows indicate the starting point region of a substantial uptake (∼40 orders of magnitude) in the production of $C_2H_2^+$ via two main channels: $e + C_2H_2 \longrightarrow C_2H_2^+ + 2e$ and $e + C_2H_4 \rightarrow H_2 + C_2H_2^+ + 2e$ (N. Endstrasser et al. 2009). This uptake in $C_2H_2^+$ thus creates a region near the cathode that is highly conducive to $C_2H_2^+$-based reactions. One of these reactions, $H + C_2H_2^+ \rightarrow CN + HCN^+$ ($k = 4.96 \times 10^{-10}$ cm^3 s^{-1}), is shown in the top right corner of the figure. The increase in reaction rate observed closer to the cathode is consistent with high $C_2H_2^+$ production in that region (symbolized by the vertical bar and arrows pointing toward the cathode). The important rise in acetylene ionization occurring

Table 3
Comparison of the Modeled Gas Phase C/N Ratio Obtained by CO-PRISM and the Experimental Solid Phase C/N Ratio Obtained with XANES for N_2–CH_4 (95–5) and N_2–CH_4–C_2H_2 (94.5–5–0.5) Plasmas (M. Nuevo et al. 2022)

C/N	Gas Phase (This Work)	Tholin (Nuevo et al. 2022)	Main Functional Groups
N_2–CH_4 (90%:10%)	5.3	1.3	C = H
N_2–CH_4–C_2H_2 (95%:5%:0.5%)	8.6	2.4	C ≡ N

Note. The main functional groups determined in the gas phase and solid phase are also given.

in this region of the plasma enables efficient formation of CN radicals, which are then available to react with CH_2NH. This uptake explains the important increase in CN and R20's reaction rate (as well as other species, as seen above) spanning several orders of magnitude.

Recently, work by J. Bourgalais et al. (2019) interestingly found that CH_2NH was the only stable nitrogen-bearing molecule formed by low-pressure EUV photochemistry experiments in N_2–CH_4 (90–10) mixtures, which was then confirmed by their 0D photochemical model. With the addition in CO-PRISM of reactions R17 and R19 (Table 2) involving the first electronically excited state of atomic nitrogen $N(^2D)$ and ammonia, respectively, we are able to corroborate the results found in J. Bourgalais et al. (2019), as well as support the formation of the protonated methanimine $CH_2NH_2^+$. Methanimine being a transient species, this highlights the role of $N(^2D)$ as a good contributor to nitrogen-bearing molecules. Despite the detection of methanimine in laboratory experiments (N. Carrasco et al. 2012; S. M. Hörst et al. 2018; J. Bourgalais et al. 2019), it has been difficult to determine its exact abundance in Titan's atmosphere (J. Bourgalais et al. 2019). Future work combining modeling, data analysis, and experiments might elucidate the abundances inferred from Cassini (V. Vuitton et al. 2007).

3.4.4. Gas-tholin Elemental Compositions and Astrochemical Implications

The unsaturated hydrocarbons shown in Figure 10 could play a crucial role in the formation of solid particles in Titan's atmosphere and are expected to contribute to the molecular diversity of *tholins* formed in COSmIC. A recent XANES analysis of tholins produced in COSmIC in N_2–CH_4 (95–5) and N_2–CH_4–C_2H_2 (94.5–5–0.5) plasmas showed the impact of C_2H_2 on the incorporation of nitrogen in the solid phase (M. Nuevo et al. 2022). We have used CO-PRISM to determine the overall elemental composition, in particular the C/N ratio, of the gas phase products in plasmas modeled with the same initial gas mixtures as the XANES study. As shown in Table 3, we observe a similar trend in C/N in the gas phase to that found in tholins; i.e., when adding acetylene, less nitrogen is being incorporated in the molecular products in both the gas and solid phase when C_2H_2 is present in the initial gas mixture, and the way nitrogen is incorporated in the chemical network changes. Nitrile bands are more prevalent with the addition of C_2H_2, controlled by C_4H_2 and HCN. As a consequence, this may result in a larger proportion of nitrile groups attached to aromatic structure, as opposed to aliphatic ones (M. Nuevo et al. 2022). These general similar trends give robustness to CO-PRISM.

Furthermore, C_2H_2 reactions with C_2H and C_4H also drive the formation of the first C4 and C6 molecules, diacetylene C_4H_2 and triacetylene C_6H_2, respectively (R. Peverati et al. 2016; E. O. Pentsak et al. 2024), as follows:

$$C_2H_2 + C_2H \longrightarrow C_4H_2 + H, \quad (24)$$

$$C_2H_2 + C_4H \longrightarrow C_6H_2 + H. \quad (25)$$

The $C_4H_2^+$ and $C_4H_3^+$ cations are important Titan tholin precursors, as was seen previously in E. Sciamma-O'Brien et al. (2014) and A. W. Raymond et al. (2018) and in Figure 4 at *m/z* 50 and 51, as well as in other Titan experimental studies (N. Carrasco et al. 2012; J. L. Berry et al. 2019; D. Dubois et al. 2019b, 2020). These C4 molecules play an intermediate role in the formation of larger linear and even cyclic tholin precursors (P. P. Bera et al. 2015; E. O. Pentsak et al. 2024). The formation of $C_4H_2^+$ occurs primarily through the ion–molecule reactions between C_2H_2 and $C_2H_2^+$ (R141 in the Appendix) and between C_2H_2 and C_2H^+ (R253). These pathways are important since the calculated abundances depend on the initial C_2H_2 concentration, and some C6 cyclic isomers may be formed according to reaction R141 (P. P. Bera et al. 2015). Meanwhile, diacetylene C_4H_2 may further react with $C_2H_5^+$ to produce C_2H_4 and $C_4H_3^+$ (R88; Appendix), thus highlighting the importance of constraining these pathways leading to the formation of key C4 Titan tholin precursors. Similarly, at *m/z* 51 and an even higher abundance, $C_4H_3^+$ is formed through reaction R141 with a branching ratio of 0.49 (P. P. Bera et al. 2015). This closed shell radical is produced at a fast rate of $\sim 10^{-9}$ cm^3 s^{-1}, and the relatively good agreement we obtain with the experimental measurements indicates that the aforementioned reaction pathways play a central role in the precursor chemistry synthesizing Titan tholins. Triacetylene C_6H_2 is found in the ISM but undetected on Titan; future work regarding its formation and subsequent loss through ion chemistry would help the understanding of the role of C6 radical chemistry toward polyyne formation, relevant to acetylene-rich *tholin* formation (J. Cernicharo et al. 2001; C. S. Contreras & F. Salama 2013; P. P. Bera et al. 2015; C. A. Nixon 2024).

The rich chemistry induced by C_2H_2 may also lead to the formation of polyynes and cyanopolyynes, first forming propiolonitrile HC_3N, to eventually C_3N or C_5N via neutral–neutral or ionic channels (D. Dubois et al. 2019a; E. O. Pentsak et al. 2024), which could help to better characterize the gas phase precursors before their incorporation into the tholins. Future incorporation of barrierless reactions other than the favorable CN + C_2H_2 or even the formation of triacetylene C_6H_2 by the reaction between diacetylene and the ethynyl radical (E. O. Pentsak et al. 2024) could assist mass spectrometry or spectroscopic measurements in identifying more precursors.

Furthermore, we may also be able to constrain our chemical network and the underlying mechanisms for ring formation (so far not accounted for in CO-PRISM) with the help of flame-burning models, which would have application not only for Titan's atmosphere but also for other astrophysical

environments, in particular, circumstellar envelopes. Several models have provided guidance to cyclization pathways via barrierless recombination reactions relevant to circumstellar envelopes (E. O. Pentsak et al. 2024). The presence of quantifiable C6 species at *m/z* 76 and 77 (Figure 4 and Section 3.1) warrants a numerical focus on low-temperature barrierless pathways for which products may be within the sensitivity range of mass spectrometry and other techniques. In any case, this gas phase investigation supports the experimental findings between the correlation of acetylene and the higher formation yield toward aromatic compounds conducted experimentally (C. S. Contreras & F. Salama 2013; E. Sciamma-O'Brien et al. 2014; M. Nuevo et al. 2022).

3.4.5. Perspectives for Future Model Expansions

Through this work, we have shown an improvement in the level of agreement between the CO-PRISM modeling and experimental TOF measurements. In particular, the computed mass spectra better reflect the experimental intensities of C2 and C3 ions and, notably now, C6 species associated with the production of benzene at *m/z* 76 and 77 when adding C_2H_2 to the gas mixture. Nonetheless, some limitations to the model are present and can be refined in future studies in order to further improve agreements with experimental measurements and guide future experiments. First, more realistic sticking coefficient values, instead of the $\gamma_k = 1$ value currently considered in CO-PRISM, could better account for surface chemistry at the walls and the potential importance of NH_3 surface chemistry. Second, including particle formation mechanisms that would deplete the gas medium of certain species, currently not included in CO-PRISM, would be a more realistic representation of what is observed experimentally, as studies have shown that tholins are formed in the COSmIC plasma discharge (e.g., E. Sciamma-O'Brien et al. 2017). The mechanisms leading to the formation of solid particles from gas precursors are, however, not yet well understood. Finally, including isotopologues and negative ions in the chemical network would lead to a more comprehensive picture of the plasma chemistry occurring in COSmIC.

4. Conclusions

Using a newly updated chemical network model, we calculated ion–neutral reactions to simulate the NASA Ames Research Center COSmIC Simulation Chamber–Titan Haze Simulation setup, a low-pressure and low-temperature supersonic plasma discharge. We conducted an analysis of N_2–CH_4-based gas phase reactivity relevant to Titan's upper atmosphere conditions and compared model outputs to experimental measurements using TOF mass spectrometry. This analysis relied on updating and expanding the reaction rates part of our reaction scheme with the latest available data. Mass spectra were computed for plasmas containing varying concentrations of CH_4 and other precursors (e.g., C_2H_2, C_2H_4). The simulated plasma composition (gas phase products, electron density and temperature, and molecular densities) was characterized in these conditions. The main results are as follows.

1. We carried out a substantial expansion on the already-existing model by adding 45 new reactions along with updating 77 other reactions according to the most recent data available in the literature. This included key electron impact ionization cross sections for hydrocarbon-based plasmas. These changes resulted in the modification of the mass distribution in the computed mass spectra, particularly (i) a better agreement with the experimental spectra for some C3, C4, and C5 species; (ii) the partial contribution of the transient and important methanimine and its protonated form $CH_2NH_2^+$ due to C_2H_2-driven chemistry; and (iii) the reproduction of experimentally detected benzene C6 fragments. These observations have helped constrain updated reactions and/or reaction rates and their respective sensitivity on the polymeric gas phase growth.
2. The polymeric growth progressing through the plasma cavity was assessed by generating spectra along the supersonic flow, giving insights on the effect small hydrocarbons have on larger hydrocarbons.
3. The role of ionization efficiency in the plasma cavity was characterized, which highlighted the influence primary ions and electrons have on the chemical inventory.
4. While updates to the reaction network have improved the level of agreement between model and experiment, we show that the chosen reactions do not yet perfectly capture the complicated evolution of the plasma. There continue to be experimental detections not observed in the model prediction, and vice versa. The high degree of sensitivity to the precursor species (like C_2H_2) has helped to assess the impact of these specific precursors, which as a result can help define which molecules or specific pathways might still be missing from our reaction scheme.
5. An intense ionization regime induced by high C_2H_2 consumption has been associated with ionic pathways leading to the formation of larger compounds (C5 and C6) and was compared with a recent study on carbonaceous nanoparticle growth by hydrocarbon addition. We obtain good agreement for abundances of $C_6H_4^+$ and $C_6H_5^+$ between experiments and computations resulting from the reaction between C_2H_2 with $C_4H_2^+$ and C_2H_2 with $C_4H_3^+$, respectively. Thus, these reactions are found to be key to explaining the presence of C6 precursor molecules of Titan tholins.
6. These changes to CO-PRISM enabled a theoretical investigation of the production of the HCN dimer, its relationship to methanimine, and nitrogen incorporation into larger intermediates such as benzonitrile precursors. These advancements were made possible by the incorporation of key reactions involving the first electronically excited state of atomic nitrogen and NH radicals, highlighting the influence of acetylene on cold, astrophysically relevant environments. While solid phase (tholin) chemistry is not taken into consideration in our calculations, only gas phase chemistry, current developments to also include negative ion chemistry and other prebiotically relevant species are underway.
7. The COSmIC experiment simulates low-temperature chemistry relevant to Titan and other planetary atmospheres. Our study aims to integrate chemical modeling with experimental measurements to identify key pathways in Titan's atmospheric chemistry within the COSmIC setup. By comparing COSmIC data with synthetic mass spectra from CO-PRISM, we can (1) validate CO-PRISM's chemical network, (2) identify and

add missing pathways or molecules, (3) quantify plasma-produced species, (4) evaluate the impact of specific pathways on chemical products, and (5) guide future COSmIC experiments to better understand Titan's atmosphere. The necessity for these targeted experiments to interpret Cassini observations was highlighted in previous research.

Acknowledgments

We thank two anonymous reviewers for their insightful comments, which contributed to improving the quality of the manuscript. Funding was provided through appointment with the NASA Postdoctoral Program and through the NASA SMD CDAP R&A Program. A portion of this work was carried out by the Jet Propulsion Laboratory, California Institute of Technology, under a contract with NASA.

Appendix

Figure 13 shows computed mass spectra in four additional conditions containing C_2H_6, NH_3, HCN, and CH_2NH in minor amounts. No notable changes >1% in these mass spectra are observed. More extensive networks including these species and their parent molecules are likely missing from our reaction scheme to explain the substantial production of new species. The absence of meaningful changes in the calculated mass spectra for these four plasma conditions could be due to (i) an incomplete list of reactions using any of these molecules as a reactant in the model or (ii) any minor species production remaining overwhelmed by CH_4-induced chemistry. In other words, any pathways related to the added minor species are eventually superseded by CH_4-induced chemistry. This could create a condition where CH_4-induced chemistry with a CH_4 concentration of 10% reaches a stage where readily available low-mass ions such as H^+, CH^+, and CH_2 preferentially participate in the production of species that would otherwise just as well be formed in a simple N_2–CH_4 model, without much influence of other minor species. In reality, it is likely that a combination of both hypotheses may explain the lack of other observed products. To remediate this issue, future work should explore the addition of new reactions involving these precursors in conjunction with experimental measurements. This is, however, outside the scope of this study. In addition, most pathways toward C_2H_6 and NH_3 production involve very slow bimolecular reactions (A. W. Raymond et al. 2018) and Table A1, compared to C_2H_2-based chemistry as seen in this study, are almost completely negligible.

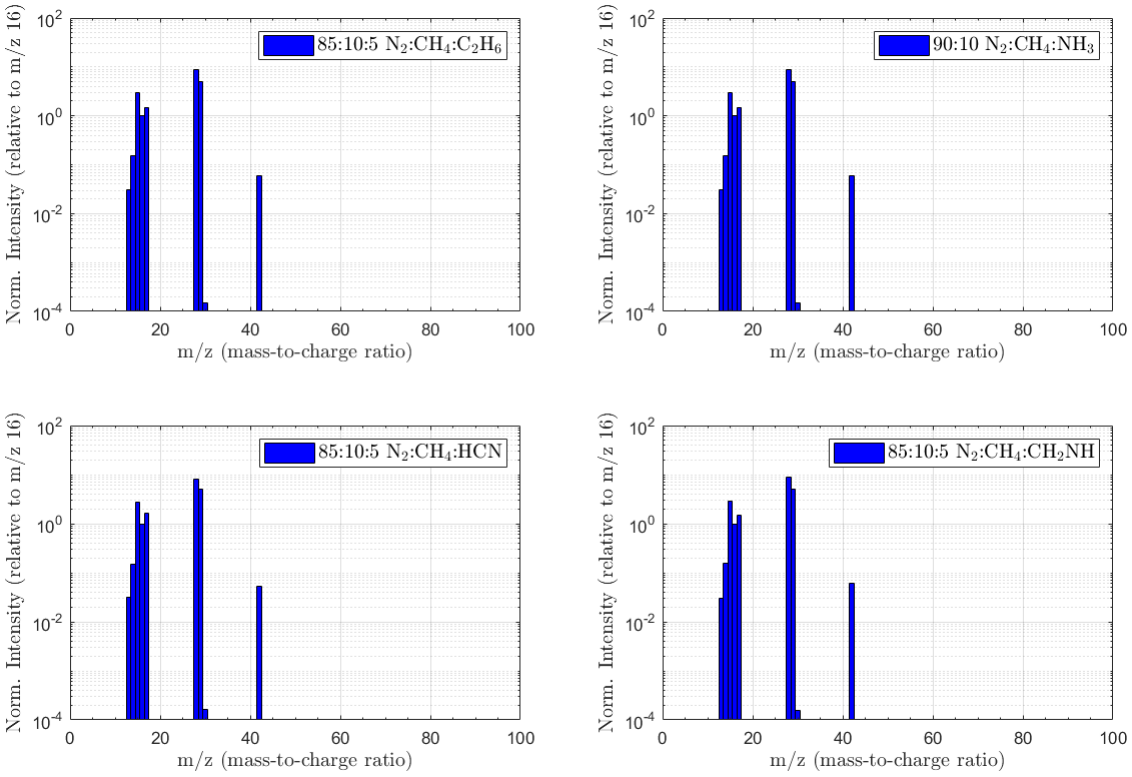

Figure 13. Mass spectra computed in N_2:CH_4:C_2H_6, N_2:CH_4:NH_3, N_2:CH_4:HCN, and N_2:CH_4:CH_2NH (85:10:5) plasma conditions. Intensities are normalized to the peak at m/z 16.

Table A1
Full Chemical Scheme Used in CO-PRISM

No.	Reaction	Rate k (cm^3 s^{-1})	Reference
1	$e + CH_4 \longrightarrow 2e + CH^+ + 3H$	$f(\epsilon)$	D. A. Erwin & J. A. Kunc (2005)
2	$e + CH_4 \longrightarrow 2e + CH_2 + 2H$	$f(\bar{\epsilon})$	D. A. Erwin & J. A. Kunc (2005)
3	$e + CH_4 \longrightarrow 2e + CH_3 + H$	$f(\bar{\epsilon})$	D. A. Erwin & J. A. Kunc (2005)
4	$e + CH_4 \longrightarrow 2e + CH_4^+$	$f(\bar{\epsilon})$	D. A. Erwin & J. A. Kunc (2005)
5	$e + CH_4 \longrightarrow e + CH + 3H$	$f(\bar{\epsilon})$	D. A. Erwin & J. A. Kunc (2005)
6	$e + CH_4 \longrightarrow e + CH_2 + H_2$	$f(\bar{\epsilon})$	D. A. Erwin & J. A. Kunc (2005)
7	$e + CH_4 \longrightarrow e + CH_3 + H$	$f(\bar{\epsilon})$	D. A. Erwin & J. A. Kunc (2005)
8	$e + C_2H_2 \longrightarrow 2e + C + CH_2^+$	$f(\bar{\epsilon})$	S. Feil et al. (2006)
9	$e + C_2H_2 \longrightarrow 2e + CH_2 + C^+$	$f(\bar{\epsilon})$	S. Feil et al. (2006)
10	$e + C_2H_2 \longrightarrow 2e + C_2H_2^+$	$f(\bar{\epsilon})$	S. Feil et al. (2006)

(This table is available in its entirety in machine-readable form in the online article.)

ORCID iDs

David Dubois https://orcid.org/0000-0001-6754-8933
Alexander W. Raymond https://orcid.org/0000-0002-0596-6336
Ella Sciamma-O'Brien https://orcid.org/0000-0002-1883-552X
Farid Salama https://orcid.org/0000-0002-6064-4401

References

Angelova, G., Novotny, O., Mitchell, J., et al. 2004, Branching Ratios for the Dissociative Recombination of Hydrocarbon Ions, IJMSp, 235, 7
Anicich, V. G. 2003, An Index of the Literature for Bimolecular Gas Phase Cation-molecule Reaction Kinetics, JPL Publications 03-19 1-1194, Jet Propulsion Laboratory
Arnold, S. T., Williams, S., Dotan, I., et al. 1999, Flow Tube Studies of Benzene Charge Transfer Reactions from 250 to 1400 K, JPCA, 103, 8421
Barone, V., & Puzzarini, C. 2022, Toward Accurate Formation Routes of Complex Organic Molecules in the Interstellar Medium: The Paradigmatic Cases of Acrylonitrile and Cyanomethanimine, FrASS, 8, 255
Bejaoui, S., Bera, P. P., Salama, F., & Lee, T. 2023, Cavity Ring-Down Spectroscopy of Anthracene, 9-Methylanthracene, and 2-Methylanthracene in Supersonic Expansion, JPCA, 127, 2717
Bejaoui, S., & Salama, F. 2019, Cavity Ring Down Spectroscopy of Cold Neutral Phenanthrene and Phenanthridine in Supersonic Jets, AIPA, 9, 085021
Benedikt, J. 2010, Plasma-chemical Reactions: Low Pressure Acetylene Plasmas, JPhD, 43, 043001
Bera, P. P., Peverati, R., Head-Gordon, M., & Lee, T. J. 2015, Hydrocarbon Growth via Ion-molecule Reactions: Acetylene and Its Fragments, PCCP, 17, 1859
Berry, J. L., Ugelow, M. S., Tolbert, M. A., & Browne, E. C. 2019, Chemical Composition of Gas-Phase Positive Ions during Laboratory Simulations of Titan's Haze Formation, ESC, 3, 202
Biennier, L., Alsayed-Ali, M., Foutel-Richard, A., et al. 2006a, Laboratory Measurements of the Recombination of PAH Ions with Electrons: Implications for the PAH Charge State in Interstellar Clouds, FaDi, 133, 289
Biennier, L., Benidar, A., & Salama, F. 2006b, Flow Dynamics of a Pulsed Planar Expansion, CP, 326, 445
Bourgalais, J., Carrasco, N., & Vettier, L. 2019, Low-Pressure EUV Photochemical Experiments: Insight on the Ion Chemistry Occurring in Titan's Atmosphere, JGRA, 124, 9214
Bourgalais, J., Carrasco, N., Vettier, L., et al. 2020, On an EUV Atmospheric Simulation Chamber to Study the Photochemical Processes of Titan's Atmosphere, NatSR, 10, 10009
Bourgalais, J., Carrasco, N., Vettier, L., et al. 2021, Aromatic Formation Promoted by Ion-Driven Radical Pathways in EUV Photochemical Experiments Simulating Titan's Atmospheric Chemistry, JPCA, 125, 3159
Broks, B. H., Brok, W. J., Remy, J., et al. 2005a, Modeling the Influence of Anode-cathode Spacing in a Pulsed Discharge Nozzle, AcSpB, 60, 1442
Broks, B. H. P., Brok, W. J. M., Remy, J., & van der Mullen, J. J. A. M. 2005b, Numerical Investigation of the Discharge Characteristics of the Pulsed Discharge Nozzle, PhRvE, 71, 036409
Cable, M. L., Hörst, S. M., Hodyss, R., et al. 2012, Titan Tholins: Simulating Titan Organic Chemistry in the Cassini-Huygens Era, ChRv, 112, 1882
Carrasco, N., Alcaraz, C., Dutuit, O., et al. 2008, Sensitivity of a Titan Ionospheric Model to the Ion-molecule Reaction Parameters, P&SS, 56, 1644
Carrasco, N., Bourgalais, J., Vettier, L., et al. 2022, A Missing Link in the Nitrogen-rich Organic Chain on Titan, A&A, 663, A165
Carrasco, N., Gautier, T., Es-Sebbar, E. T., Pernot, P., & Cernogora, G. 2012, Volatile Products Controlling Titan's Tholins Production, Icar, 219, 230
Cernicharo, J., Heras, A. M., Tielens, A. G. G. M., et al. 2001, Infrared Space Observatory's Discovery of C4H2, C6H2, and Benzene in CRL 618, ApJL, 546, L123
Contreras, C. S., & Salama, F. 2013, Laboratory Investigations of Polycyclic Aromatic Hydrocarbon Formation and Destruction in the Circumstellar Outflows of Carbon Stars, ApJS, 208, 6
Coustenis, A., Schmitt, B., Khanna, R. K., & Trotta, F. 1999, Plausible Condensates in Titan's Stratosphere from Voyager Infrared Spectra, P&SS, 47, 1305
Couturier-Tamburelli, I., Gudipati, M. S., Lignell, A., Jacovi, R., & Piétri, N. 2014, Spectroscopic Studies of Non-volatile Residue Formed by Photochemistry of Solid C4N2: A Model of Condensed Aerosol Formation on Titan, Icar, 234, 81
Crary, F. J., Magee, B. A., Mandt, K., et al. 2009, Heavy Ions, Temperatures and Winds in Titan's Ionosphere: Combined Cassini CAPS and INMS Observations, P&SS, 57, 1847
Cui, J., Galand, M., Yelle, R. V., et al. 2009a, Diurnal Variations of Titan's Ionosphere, JGRA, 114, A06310
Cui, J., Yelle, R. V., Vuitton, V., et al. 2009b, Analysis of Titan's Neutral Upper Atmosphere from Cassini Ion Neutral Mass Spectrometer Measurements, Icar, 200, 581
De Bleecker, K., Bogaerts, A., & Goedheer, W. 2006a, Aromatic Ring Generation as a Dust Precursor in Acetylene Discharges, ApPhL, 88, 151501
De Bleecker, K., Bogaerts, A., & Goedheer, W. 2006b, Detailed Modeling of Hydrocarbon Nanoparticle Nucleation in Acetylene Discharges, PhRvE, 73, 026405
Dinelli, B. M., Adriani, A., Moriconi, M. L., Funke, B., & Aversa, E. D. 2013, An Unidentified Emission in Titan's Upper Atmosphere, GeoRL, 40, 1489
Dobrijevic, M., Loison, J. C., Hickson, K. M., & Gronoff, G. 2016, 1D-coupled Photochemical Model of Neutrals, Cations and Anions in the Atmosphere of Titan, Icar, 268, 313
Dubois, D. 2025, Photochemical Haze Formation on Titan and Uranus: A Comparative Review, IJMSc, 26, 7531
Dubois, D., Carrasco, N., Bourgalais, J., et al. 2019a, Nitrogen-containing Anions and Tholin Growth in Titan's Ionosphere: Implications for Cassini CAPS-ELS Observations, ApJL, 872, L31
Dubois, D., Carrasco, N., Jovanovic, L., et al. 2020, Positive Ion Chemistry in an N2-CH4 Plasma Discharge: Key Precursors to the Growth of Titan Tholins, Icar, 338, 113437
Dubois, D., Carrasco, N., Petrucciani, M., et al. 2019b, In Situ Investigation of Neutrals Involved in the Formation of Titan Tholins, Icar, 317, 182

Dutuit, O., Carrasco, N., Thissen, R., et al. 2013, Critical Review of N, N+, N2+, N++, and N++2 Main Production Processes and Reactions of Relevance to Titan's Atmosphere, ApJS, 204, 20
Endstrasser, N., Zappa, F., Mauracher, A., et al. 2009, Absolute Partial Cross Sections and Kinetic Energy Analysis for the Electron Impact Ionization of Ethylene, IJMSp, 280, 65
Erwin, D. A., & Kunc, J. A. 2005, Electron-impact Dissociation of the Methane Molecule Into Neutral Fragments, PhRvA, 72, 052719
Esposito, V., Alessandrini, S., & Dubois, D. 2025, A Catalytic Pathway for the Formation of Cyanobenzene in Nitrogen-rich Environments and the Spectroscopy of the Reactive Intermediates, PSJ, 6, 113
Feil, S., Głuch, K., Bacher, A., et al. 2006, Cross Sections and Ion Kinetic Energy Analysis for the Electron Impact Ionization of Acetylene, JChPh, 124, 214307
Ferus, M., Kubelík, P., Knížek, A., et al. 2017, High Energy Radical Chemistry Formation of HCN-rich Atmospheres on Early Earth, NatSR, 7, 6275
Fortenberry, R. C., & Esposito, V. J. 2024, On the Formation and Detectability of H 2 CNCN and Its Progenitors, ApJ, 972, 35
Freeman, C., Harland, P., & McEwan, M. 1978, The Interstellar Synthesis of HC3N and HC5N, ApL, 19, 133
Geppert, W. D., Thomas, R., Semaniak, J., et al. 2004, Dissociative Recombination of N_2H^+: Evidence for Fracture of the NN Bond, ApJ, 609, 459
Gu, X., Kaiser, R. I., Mebel, A. M., et al. 2009, A Crossed Molecular Beams Study on the Formation of the Exotic Cyanoethynyl Radical in Titan's Atmosphere, ApJ, 701, 1797
Hagelaar, G. J., & Pitchford, L. C. 2005, Solving the Boltzmann Equation to Obtain Electron Transport Coefficients and Rate Coefficients for Fluid Models, PSST, 14, 722
Harada, N., Herbst, E., & Wakelam, V. 2010, A New Network for Higher-Temperature Gas-Phase Chemistry. I. A Preliminary Study of Accretion Disks in Active Galactic Nuclei, ApJ, 721, 1570
Harrison, R. G., & Tammet, H. 2008, Ions in the Terrestrial Atmospheres and Other Solar System Atmospheres, Planetary Atmospheric Electricity, Vol. 30 (Berlin: Springer), 107
Hébrard, E., Dobrijevic, M., Pernot, P., et al. 2009, How Measurements of Rate Coefficients at Low Temperature Increase the Predictivity of Photochemical Models of Titan's Atmosphere, JPCA, 113, 11227
Hörst, S. M., Yoon, Y. H., Ugelow, M. S., et al. 2018, Laboratory Investigations of Titan Haze Formation: In Situ Measurement of Gas and Particle Composition, Icar, 301, 136
Huntress, W. T. 1977, Ion-molecule Reactions in the Evolution of Simple Organic Molecules in Interstellar Clouds and Planetary Atmospheres, CSRev, 6, 295
Huo, W. M., Liu, Y., Panesi, M., et al. 2015, Electron-impact Excitation Cross Sections for Modeling Non-equilibrium Gas, AIAA Aerospace Sciences Meeting, 53, 1
Imanaka, H., Khare, B. N., Elsila, J. E., et al. 2004, Laboratory Experiments of Titan Tholin Formed in Cold Plasma at Various Pressures: Implications for Nitrogen-containing Polycyclic Aromatic Compounds in Titan Haze, Icar, 168, 344
Janalizadeh, S., Foroutan, G., & Foroutan, V. 2023, Nucleation of Carbonaceous Nanoparticles in a Low Pressure Ar/C_2H_2 Plasma with C_2H_4 Impurity, JPCA, 127, 6999
Jose, J., Zamir, A., & Stein, T. 2021, Molecular Dynamics Reveals Formation Path of Benzonitrile and Other Molecules in Conditions Relevant to the Interstellar Medium, PNAS, 118, e2101371118
Krasnopolsky, V. A. 2014, Chemical Composition of Titan's Atmosphere and Ionosphere: Observations and the Photochemical Model, Icar, 236, 83
Larsson, M., Geppert, W. D., & Nyman, G. 2012, Ion Chemistry in Space, RPPh, 75, 066901
Lavvas, P., Yelle, R. V., Koskinen, T., et al. 2013, Aerosol Growth in Titan's Ionosphere, PNAS, 110, 2729
Loison, J. C., Dobrijevic, M., Hickson, K. M., & Heays, A. N. 2017, The Photochemical Fractionation of Oxygen Isotopologues in Titan's Atmosphere, Icar, 291, 17
López-Puertas, M., Dinelli, B. M., Adriani, A., et al. 2013, Large Abundances of Polycyclic Aromatic Hydrocarbons in Titan's Upper Atmosphere, ApJ, 770, 132
Mao, M., Benedikt, J., Consoli, A., & Bogaerts, A. 2008, New Pathways for Nanoparticle Formation in Acetylene Dusty Plasmas: A Modeling Investigation and Comparison with Experiments, JPhD, 41, 225201
Marin, L. G., Bejaoui, S., Haggmark, M., et al. 2020, Low-temperature Formation of Carbonaceous Dust Grains from PAHs, ApJ, 889, 101
McEwan, M. J., & Anicich, V. G. 2007, Titan's Ion Chemistry: A Laboratory Perspective, MSRv, 26, 281
Motz, H., & Wise, H. 1960, Diffusion and Heterogeneous Reaction. III. Atom Recombination at a Catalytic Boundary, JChPh, 32, 1893
Mukundan, V., & Bhardwaj, A. 2018, A Model for Negative Ion Chemistry in Titan's Ionosphere, ApJ, 856, 168
Mullen, C., & Smith, M. A. 2005, Low Temperature NH(X 3Σ -) Radical Reactions with NO, Saturated, and Unsaturated Hydrocarbons Studied in a Pulsed Supersonic Laval Nozzle Flow Reactor between 53 and 188 K, JPCA, 109, 1391
Nixon, C. A. 2024, The Composition and Chemistry of Titan's Atmosphere, ESC, 8, 406
Noble, J. A., Theule, P., Borget, F., et al. 2013, The Thermal Reactivity of HCN and NH3 in Interstellar Ice Analogues, MNRAS, 428, 3262
Nuevo, M., Sciamma-O'Brien, E., Sandford, S. A., et al. 2022, The Titan Haze Simulation (THS) Experiment on COSmIC. Part III. XANES Study of Laboratory Analogs of Titan Tholins, Icar, 376, 114841
O'Brien, E. S., Raymond, A. W., Dubois, D., Mazur, E., & Salama, F. 2019, The Titan Haze Simulation Experiment: Investigating Titan's Low-temperature Atmospheric Chemistry in a Pulsed Plasma Jet Expansion, in IAU Symp. 350, Laboratory Astrophysics: From Observations to Interpretation (Cambridge: Cambridge Univ. Press), 410
Orgel, L. E. 2002, Is Cyanoacetylene Prebiotic?, OLEB, 32, 279
Pentsak, E. O., Murga, M. S., & Ananikov, V. P. 2024, Role of Acetylene in the Chemical Evolution of Carbon Complexity, ESC, 8, 798
Peverati, R., Bera, P. P., Lee, T. J., & Head-Gordon, M. 2016, Insights into Hydrocarbon Chain and Aromatic Ring Formation in the Interstellar Medium: Computational Study of the Isomers of and their Formation Pathways, ApJ, 830, 128
Phelps, A. V., & Petrovic, Z. L. 1999, Cold-cathode Discharges and Breakdown in Argon: Surface and Gas Phase Production of Secondary Electrons, PSST, 8, R21
Pilling, S., Andrade, D. P., Neto, A. C., Rittner, R., & De Brito, A. N. 2009, DNA Nucleobase Synthesis at Titan Atmosphere Analog by Soft X-rays, JPCA, 113, 11161
Pintassilgo, C. D., Loureiro, J., Cernogora, G., & Touzeau, M. 1999, Methane Decomposition and Active Nitrogen in a N2-CH4 Glow Discharge at Low Pressures, PSST, 463
Plessis, S., Carrasco, N., & Pernot, P. 2010, Knowledge-based Probabilistic Representations of Branching Ratios in Chemical Networks: The Case of Dissociative Recombinations, JChPh, 133, 134110
Raulin, F., Brassé, C., Poch, O., & Coll, P. 2012, Prebiotic-like Chemistry on Titan, CSRev, 41, 5380
Raymond, A. W., Sciamma-O'Brien, E., Salama, F., & Mazur, E. 2018, A Model of Titan-like Chemistry to Connect Experiments and Cassini Observations, ApJ, 853, 107
Remy, J. R. M., Biennier, L., & Salama, F. 2003, Plasma Structure in a Pulsed Discharge Environment, PSST, 12, 295
Ricketts, C. L., Contreras, C. S., Walker, R. L., & Salama, F. 2011, The Coupling of a Reflectron Time-of-flight Mass Spectrometer with a Cosmic Simulation Chamber: A Powerful New Tool for Laboratory Astrophysics, IJMSp, 300, 26
Rimmer, P. B., Majumdar, L., Priyadarshi, A., Wright, S., & Yurchenko, S. N. 2021, Detectable Abundance of Cyanoacetylene (HC 3 N) Predicted on Reduced Nitrogen-rich Super-Earth Atmospheres, ApJL, 921, L28
Ritson, D. J., Poplawski, M. W., Bond, A. D., & Sutherland, J. D. 2022, Azoles as Auxiliaries and Intermediates in Prebiotic Nucleoside Synthesis, JAChS, 144, 19447
Rosi, M., Skouteris, D., Casavecchia, P., et al. 2018, Formation of Nitrogen-Bearing Organic Molecules in the Reaction NH++C2H5: A Theoretical Investigation and Main Implications for Prebiotic Chemistry in Space, in Computational Science and Its Applications – ICCSA 2018 (Berlin: Springer), 773
Sagan, C., Thompson, W. R., & Khare, B. N. 1992, Titan: A Laboratory for Prebiological Organic Chemistry, Acc. Chem. Res., 25, 286
Salama, F., Contreras, C., Sciamma-O'Brien, E., & Bejaoui, S. 2017, Recent Progresses in Laboratory Astrophysics with Ames COSmIC Facility, in IAU Symp. 332, Astrochemistry VII: Through the Cosmos from Galaxies to Planets (Cambridge: Cambridge Univ. Press), 364
San Andrés, D., Rivilla, V. M., Colzi, L., et al. 2024, First Detection in Space of the High-energy Isomer of Cyanomethanimine: H 2 CNCN, ApJ, 967, 39
Scattergood, T. W., McKay, C. P., Borucki, W. J., et al. 1989, Production of Organic Compounds in Plasmas: A Comparison Among Electric Sparks, Laser-induced Plasmas, and UV Light, Icar, 81, 413

Sciamma-O'Brien, E., Raymond, A., Dubois, D., Mazur, E., & Salama, F. 2020, The Titan Haze Simulation Experiment: Investigating Titan's Low-temperature Atmospheric Chemistry in a Pulsed Plasma Jet Expansion, in IAU Symp. 350, Laboratory Astrophysics: From Observations to Interpretation, ed. F. Salama & H. Linnartz (Cambridge: Cambridge Univ. Press), 410

Sciamma-O'Brien, E., Ricketts, C. L., & Salama, F. 2014, The Titan Haze Simulation Experiment on cOsmic: Probing Titan's Atmospheric Chemistry at Low Temperature, Icar, 243, 325

Sciamma-O'Brien, E., Roush, T. L., Rannou, P., Dubois, D., & Salama, F. 2023, First Optical Constants of Laboratory-generated Organic Refractory Materials (Tholins) Produced in the NASA Ames COSmIC Facility from the Visible to the Near Infrared (0.4–1.6 μm): Application to Titan's Aerosols, PSJ, 4, 121

Sciamma-O'Brien, E., Upton, K. T., & Salama, F. 2017, The Titan Haze Simulation (THS) Experiment on COSmIC. Part II. Ex-situ Analysis of Aerosols Produced at Low Temperature, Icar, 289, 214

Shapiro, R. 1999, Prebiotic Cytosine Synthesis: A Critical Analysis and Implications for the Origin of Life, PNAS, 96, 4396

Singh, P. C., Shen, L., Zhou, J., Schlegel, H. B., & Suits, A. G. 2010, Photodissociation Dynamics of Methylamine Cation and Its Relevance To Titan's Ionosphere, ApJ, 710, 112

Snell, R. L., Schloerb, F. P., & Young, J. S. 1981, Observations of HC3N, HC5N, AND HC7N in Molecular Clouds, ApJ, 244, 45

Stein, T., Bera, P. P., Lee, T. J., & Head-Gordon, M. 2020, Molecular Growth Upon Ionization of van der Waals Clusters Containing HCCH and HCN is a Pathway to Prebiotic Molecules, PCCP, 20337

Stoykov, S., Eggs, C., & Kortshagen, U. 2001, Plasma Chemistry and Growth of Nanosized Particles in a C2H2 RF Discharge, JPhD, 34, 2160

Szopa, C., Cernogora, G., Boufendi, L., Correia, J. J., & Coll, P. 2006, PAMPRE: A Dusty Plasma Experiment for Titan's Tholins Production and Study, P&SS, 54, 394

Tan, X., & Salama, F. 2005, Cavity Ring-down Spectroscopy and Theoretical Calculations of the S 1(1B 3u)?S 0(1A g) Transition of Jet-cooled Perylene, JChPh, 122, 084318

Tanarro, I., Herrero, V. J., Islyaikin, A. M., et al. 2007, Ion Chemistry in Cold Plasmas of H2 with CH4 and N2, JPCA, 111, 9003

Teanby, N. A., Irwin, P. G. J., de Kok, R., et al. 2006, Latitudinal Variations of HCN, HC3N, and C2 N2 in Titan's Stratosphere Derived from Cassini CIRS Data, Icar, 181, 243

Theule, P., Borget, F., Mispelaer, F., et al. 2011, Hydrogenation of Solid Hydrogen Cyanide HCN and Methanimine CH2NH at Low Temperature, A&A, 534, A64

Tian, C., & Vidal, C. R. 1998, Cross Sections of the Electron Impact Dissociative Ionization of CO, CH4 and C2H2, JPhB, 31, 895

Vazart, F., Latouche, C., Skouteris, D., Balucani, N., & Barone, V. 2015, Cyanomethanimine Isomers in Cold Interstellar Clouds: Insights from Electronic Structure and Kinetic Calculations, ApJ, 810, 111

Vinatier, S., Schmitt, B., Bézard, B., et al. 2018, Study of Titan's Fall Southern Stratospheric Polar Cloud Composition with Cassini/CIRS: Detection of Benzene Ice, Icar, 310, 89

Vuitton, V., Yelle, R. V., & Cui, J. 2008, Formation and Distribution of Benzene on Titan, JGRE, 113, E05007

Vuitton, V., Yelle, R. V., & McEwan, M. J. 2007, Ion Chemistry and N-containing Molecules in Titan's Upper Atmosphere, Icar, 191, 722

Vuitton, V., Yelle, V., Klippenstein, S. J., Hörst, S. M., & Lavvas, P. 2019, Simulating the Density of Organic Species in the Atmosphere of Titan with a Coupled Ion-neutral Photochemical Model, Icar, 324, 120

Waite, J. H., Young, D., Cravens, T. E., et al. 2007, The Process of Tholin Formation in Titan's Upper Atmosphere, Sci, 316, 870

Wakelam, V., Herbst, E., Loison, J. C., et al. 2012, A Kinetic Database for Astrochemistry (KIDA), ApJS, 199, 21

Wong, M. L., Prabhu, A., Williams, J., Morrison, S. M., & Hazen, R. M. 2023, Toward Network-Based Planetary Biosignatures: Atmospheric Chemistry as Unipartite, Unweighted, Undirected Networks, JGR, 128, e2022JE007658

Yelle, R. V., Vuitton, V., Lavvas, P., et al. 2010, Formation of NH3 and CH2NH in Titan's Upper Atmosphere, FaDi, 147, 31

Žabka, J., Polášek, M., Ascenzi, D., et al. 2009, Reactivity of C2H5+with Benzene: Formation of Ethylbenzenium Ions and Implications for Titan's Ionospheric Chemistry, JPCA, 113, 11153

Žabka, J., Romanzin, C., Alcaraz, C., & Polášek, M. 2012, Anion Chemistry on Titan: A Possible Route to Large N-bearing Hydrocarbons, Icar, 219, 161